UNIVERSIDAD NACIONAL AUTÓNOMA DE MÉXICO
POSGRADO EN CIENCIAS FÍSICAS
INSTITUTO DE CIENCIAS NUCLEARES

TOPOLOGICAL DEFECTS IN THE O(2) MODEL OUT OF EQUILIBRIUM

TESIS
QUE PARA OPTAR POR EL GRADO DE:
MAESTRO EN CIENCIAS (FÍSICA)

PRESENTA:

JAIME FABIÁN NIETO CASTELLANOS

TUTOR:
DR. WOLFGANG PETER BIETENHOLZ
INSTITUTO DE CIENCIAS NUCLEARES

MIEMBROS DEL COMITÉ TUTOR:
DRA. LIBERTAD BARRÓN PALOS
INSTITUTO DE FÍSICA
DR. YURI BONDER GRIMBERG
INSTITUTO DE CIENCIAS NUCLEARES

CIUDAD UNIVERSITARIA, CDMX, DICIEMBRE, 2023

PROTESTA UNIVERSITARIA DE INTEGRIDAD Y HONESTIDAD ACADÉMICA Y PROFESIONAL
(Graduación con trabajo escrito)

De conformidad con lo dispuesto en los artículos 87, fracción V, del Estatuto General, 68, primer párrafo, del Reglamento General de Estudios Universitarios y 26, fracción I, y 35 del Reglamento General de Exámenes, me comprometo en todo tiempo a honrar a la Institución y a cumplir con los principios establecidos en el Código de Ética de la Universidad Nacional Autónoma de México, especialmente con los de integridad y honestidad académica.

De acuerdo con lo anterior, manifiesto que el trabajo escrito titulado:

Topological defects in the O(2) model out of equilibrium

que presenté para obtener el grado de -----Maestria----- es original, de mi autoría y lo realicé con el rigor metodológico exigido por mi programa de posgrado, citando las fuentes de ideas, textos, imágenes, gráficos u otro tipo de obras empleadas para su desarrollo.

En consecuencia, acepto que la falta de cumplimiento de las disposiciones reglamentarias y normativas de la Universidad, en particular las ya referidas en el Código de Ética, llevará a la nulidad de los actos de carácter académico administrativo del proceso de graduación.

Jaime Fabián

Atentamente

Jaime Fabián Nieto Castellanos
314244136

(Nombre, firma y Número de cuenta de la persona alumna)

Abstract

We present a study of the 2- and 3-dimensional XY model, or O(2) model, out of equilibrium through Monte Carlo simulations. In particular, we analyze the dynamics of the topological defects of the system (vortices) when we linearly lower the temperature at various cooling rates, starting above the critical temperature, T_c, down to $T < T_c$. In 3 dimensions we test Zurek's prediction for the scaling behavior of the density of topological defects that remains after a cooling procedure for a system that undergoes a second order phase transition. We find that the remnant density depends on the cooling rate with a power-law, in partial agreement with Zurek's prediction. This property is independent of the Monte Carlo algorithm that we choose. Still, the exact scaling behavior depends on the algorithm. A power-law has also been observed in experiments of systems with continuous phase transitions. This approach could be extended to estimate the density of cosmic strings that persists from the expansion and cooling of the early universe, by simulating different models.

Resumen

Se presenta un estudio del modelo XY, o modelo O(2), en dos y tres dimensiones, a través de simulaciones Monte Carlo fuera del equilibrio. En particular, se analiza la dinámica de los defectos topológicos del sistema (vórtices) cuando la temperatura se reduce linealmente a diferentes tasas de enfriamiento, iniciando arriba de la temperatura crítica, T_c, y terminando en $T < T_c$. En tres dimensiones se pone a prueba la predicción dada por Zurek para el escalamiento de la densidad de los defectos topológicos que queda después de un proceso de enfriamiento para un sistema que sufre una transición de fase de segundo orden. Se encuentra que la densidad remanente depende de la tasa de enfriamiento con una ley de potencia, en acuerdo parcial con la predicción de Zurek. Esta propiedad es independiente del algoritmo Monte Carlo que se escoja. Aún así, el escalamiento exacto, dado por el exponente de la ley de potencia, depende del algoritmo. También se ha observado una ley de potencia en experimentos de sistemas con transiciones de fase continuas. Este enfoque puede ser extendido para estimar la densidad de cuerdas cósmicas que persiste de la expansión y el enfriamiento del universo temprano, a través de simulaciones de distintos modelos.

Acknowledgments

First of all, I would like to thank my advisor, Dr. Wolfgang Bietenholz, for inviting me to collaborate in this project and for thoroughly proofreading and helping me to improve this thesis. I am also very grateful to my colleagues Edgar López and Elías Polanco, for allowing me to confront my simulation results with theirs. In addition, I thank Edgar for showing me the implementation of the heatbath algorithm, which is used in this work.

Agradezco a mis padres, Alma y Jaime, por dejarme estudiar lo que yo quisiera y por aguantarme dos años más en la casa mientras estudiaba mi maestría.

Agradezco a Claudio Allen, por una amistad de más de 20 años. Asimismo, agradezco también a César Álvarez, Daniel Núñez y Martín Ibarra, por su amistad durante la licenciatura y el posgrado. Adicionalmente, agradezco a Martín por permitirme ser su ayudante en la licenciatura.

Finalmente, agradezco al Consejo Nacional de Humanidades, Ciencias y Tecnologías (CONAHCYT) por la beca otorgada durante mis estudios de posgrado, así como a la UNAM, por la beca otorgada a través del proyecto DGAPA-PAPIIT "Materia fuertemente acoplada en condiciones extremas con el MPD-NICA", con clave CG100322, durante la realización de esta tesis. Sin embargo, agradezco principalmente a la gente que paga impuestos en México, porque me han dado educación gratuita y de calidad desde la preparatoria. La educación es un derecho, no un privilegio.

Contents

Introduction

The established theories assume that the early universe underwent several phase transitions during its rapid expansion and cooling, immediately after the Big Bang. Possible remnants of these transitions are *topological defects*, which are field configurations that may persist under cooling and symmetry breaking. There are different types of topological defects that emerge, depending on the symmetry breaking pattern. This has been studied in detail by Kibble [1]. Some of these defects might have persisted until today and current observations suggest that *cosmic strings* are the best candidate to be observed in the future, through experiments like the Laser Interferometer Space Antenna (LISA) [2]. The idea is to detect the gravitational radiation that excitations of cosmic strings loops could emit.

To theoretically study cosmic strings formation, it is standard to simulate systems that exhibit this kind of defects. In particular, the classical XY, or O(2), model is a convenient option. Its three-dimensional version undergoes a second order phase transition and contains vortices as topological defects. The vortices can be connected to create vortex lines which may generate large networks, analogous to the ones that cosmic strings could form. Studying the creation of these networks in equilibrium might not be useful to estimate the current density of cosmic strings in the universe, because of the cooling and expansion of the latter. Therefore, simulations of the dynamics of these networks during a cooling process, that passes through the phase transition from $T > T_c$ down to $T < T_c$, are suitable. If the cooling is very slow, the system is quasi-adiabatic. However, the phase transition naturally leads to the loss of equilibrium in the vicinity of the critical point. Some generic properties of a system that undergoes a second order phase transition during a linear cooling at different rates were predicted by Zurek [3]. Specifically, he gives an estimate for the density of topological defects that persists at the transition time between the region in equilibrium and the region out of equilibrium. He mentions that the density of topological defects should scale with a power-law in the inverse cooling rate. In addition, an scaling exponent is given. His work has been experimentally tested in different settings [4–6]. The power-law is always observed, but there is no consensus regarding the scaling exponent.

In this thesis we study the dynamics of the vortex density of the two- and three-dimensional XY model by means of Monte Carlo simulations. We attempt to verify Zurek's prediction by systematically applying distinct algorithms to simulate the evolution of the vortex density during a linear cooling process. For this purpose, we use the *Metropolis* and *heatbath* algorithms, which are local-update schemes. All the codes were self-written in C++.

The structure of this thesis is the following:

- Chapter 1: We review the Kibble mechanism and show some examples of the emergence of topological defects in different theories. At the end of the chapter, we review the prediction by Zurek for the density of topological defects.

- Chapter 2: We review the classical XY model in two and three dimensions. In the two-dimensional version, we discuss the importance of the vortices to explain the so-called BKT transition. We also give the relevant features of the three-dimensional version of the model.
- Chapter 3: We describe the basic concepts of Markov chains, which are needed to understand the working of *importance sampling* Monte Carlo simulations. We review some technical aspects of these simulations, together with the implementation of four different algorithms to simulate the XY model.
- Chapter 4: We present simulation results of the two-dimensional XY model in equilibrium and out of equilibrium, performed with different algorithms. The results are compared with the literature.
- Chapter 5: We present simulation results of the three-dimensional XY model. We attempt to verify Zurek's prediction for the scaling of the topological defects during a linear cooling process. We use the algorithms Metropolis and heatbath.
- Chapter 6: We summarize the work and present our conclusions.

Chapter 1

The Kibble-Zurek mechanism

Symmetry breaking and phase transitions play an important role in the understanding of numerous physical phenomena. Examples include the spontaneous organization and structuring of the water molecules in the liquid to ice transition, all the way to the Higgs mechanism, which explains the masses of the elementary particles of the Standard Model. It is also standard to assume that the early universe, after the Big Bang (10^{-35} s – 10^{-11} s), underwent several phase transitions that broke some symmetries during its rapid expansion and cooling. A review of phase transitions in the early universe is given in Ref. [7].

Evidence of such transitions could possibly be found by searching for *topological defects*. These are configurations that form in the symmetric phase before a transition. They come in a variety of types, such as domain walls, cosmic strings or monopoles. After a cooling process, some of these defects could have survived and might even be detectable today. Such structures are well known in condensed matter systems; nevertheless, their existence in the cosmos is only hypothetical. Still, the appearance of some of the defects previously mentioned is unlikely due to contradictions with current observations. Until now, cosmic strings are considered the best candidate to be observed in the future. These strings could connect and form large loops throughout the cosmos. Excitations of these loops would generate gravitational waves that could be detected. Upcoming experiments, like the Laser Interferometer Space Antenna (LISA), are expected to provide some insight in this regard. According to Ref. [2], the power spectra of some cosmic strings models could be observed in LISA's frequency detection range (0.1 mHz − 1 Hz).

In the following section, we briefly describe the mechanism through which topological defects might form.

1.1 The Kibble mechanism

In 1976, Kibble presented a mechanism that explains the formation of topological defects in the early universe [1]. To review the idea, we consider a model with a complex scalar field, $\phi(x) \in \mathbb{C}$, at finite temperature, described by the Lagrangian

$$\mathcal{L} = \frac{1}{2}\partial_\mu \phi^\dagger \partial^\mu \phi - \frac{1}{2}m_0^2|\phi|^2 - \frac{\lambda}{4!}|\phi|^4, \tag{1.1}$$

with $m_0^2 < 0$ and $\lambda > 0$. Note that this Lagrangian has a global U(1) symmetry, $\phi(x) \to \exp(i\alpha)\phi(x)$. If one computes the effective potential to one loop, the m_0^2 parameter acquires

a correction due to the temperature (see Ref. [8] or Chapter 6 of [9])

$$V_{\text{eff}}(|\phi|) = \frac{1}{2}m^2(T)|\phi|^2 + \frac{\lambda}{4!}|\phi|^4, \quad m^2(T) = m_0^2\left(1 + \frac{T^2\lambda}{24m_0^2} + \mathcal{O}(\lambda^2)\right). \tag{1.2}$$

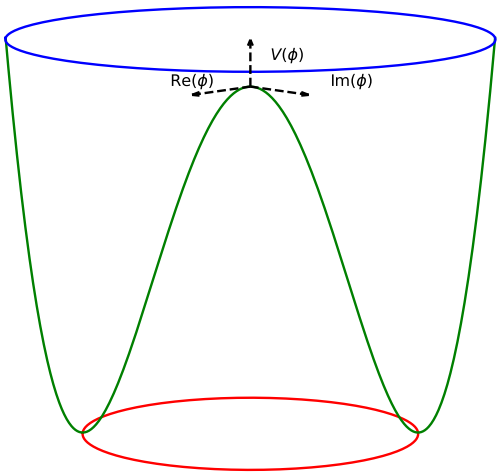

Figure 1.1: Effective potential (1.2) for $m^2 < 0$. We see that the classical ground state is degenerate, there is a full circle of minima.

For temperatures $T > T_c \equiv \sqrt{-24m_0^2/\lambda}$ (at one loop), the m^2 parameter is positive and the potential has a global minimum at $\phi = 0$. This means that for $T > T_c$ the ground state is unique and symmetric with respect to U(1) transformations. However, for $T < T_c$ the value of m^2 is negative, which in turn changes the shape of the potential, as depicted in Figure 1.1. In this situation, the classical ground state is found when the vacuum expectation value of ϕ takes the form

$$\langle\phi\rangle = \sqrt{\frac{-6m^2(T)}{\lambda}}e^{i\theta}, \quad \theta \in [0, 2\pi). \tag{1.3}$$

Then, if one fixes a value of θ, we observe that the ground state is not U(1) symmetric anymore, which means that the symmetry is spontaneously broken.

In his seminal work, Kibble [1] proposed that at early stages of the universe, when it was very hot and dense, a number of symmetries were unbroken. As it expanded and cooled, they broke. However, at some time t, distances separated by more than ct were not causally connected anymore. Therefore, the vacuum expectation value of ϕ could take different phases θ for disconnected regions. As a consequence, the universe acquired a domain structure similar to the one of ferromagnets. The size of these domains is related to the *correlation length* ξ, which is defined through the decay of the connected correlation function

$$\langle\phi(x)\phi(y)\rangle_c \sim e^{-|x-y|/\xi}. \tag{1.4}$$

In this situation, different types of topological defects can arise in the boundaries between the domains. This entire process is known as the *Kibble mechanism*.

Refs. [1,10] also show that, depending on the symmetry breaking pattern, it is possible to classify the topological defects that the theory possesses in terms of homotopy groups.

1.2 Topological defects

In this section, we present examples of theories where topological defects form. In all of them, the defects appear as a consequence of the breaking of a symmetry.

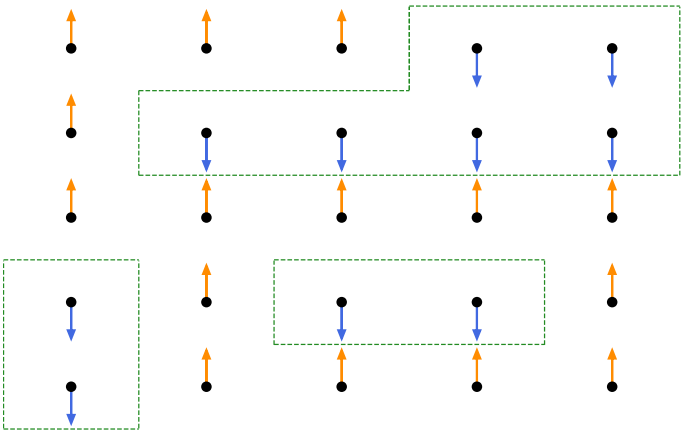

Figure 1.2: Schematic representation of an Ising ferromagnet at $T < T_c$. We observe that the system divides into domains, separated by walls (green dashed lines).

1.2.1 Domain walls

We first introduce the domain walls by considering an Ising ferromagnetic material, described by the following classical Hamiltonian

$$H = -J \sum_{\langle ij \rangle} S_i S_j, \quad S_i \in \{-1, 1\}, \tag{1.5}$$

where J is a coupling constant and the sum runs over the nearest neighbors of a cubic lattice with N sites, see Figure 1.2. For a temperature higher than the critical value, $T > T_c$, the material loses its magnetic properties, because the spins are, for the most part, randomly oriented. For $T < T_c$ in equilibrium, the spins tend to align in regions with uniform orientations and there is a non-zero overall magnetization. These regions are known as domains and their boundaries are referred to as walls. In this example and for dimension $d > 2$, the $\mathbb{Z}^2$ symmetry (changing $S_i \to -S_i$) is spontaneously broken below the critical temperature, since for $T < T_c$ the reflection symmetry is broken within the domains and the overall magnetization is non-zero. It is important to mention that the contribution to the energy above its minimum value is contained in the walls. To see this, we introduce the following variable between two neighbouring sites

$$n_{ij} = \frac{1 - S_i S_j}{2} = \begin{cases} 1 & \text{if there is a wall between } S_i \text{ and } S_j, \\ 0 & \text{otherwise.} \end{cases} \tag{1.6}$$

Substituting n_{ij} in eq. (1.5) yields

$$H = -NdJ + 2J \sum_{\langle ij \rangle} n_{ij}, \tag{1.7}$$

where d is the system's dimension. Thus, each element of a wall contributes a factor $2J$ to H and they carry the system's energy, above the minimum.

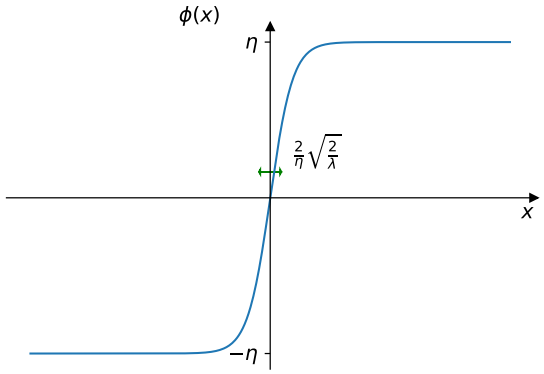

Figure 1.3: Solution to the classical equations of motion of the Lagrangian (1.8). The green arrow indicates the width of the kink, which carries most of the energy.

Another example where this type of topological defects emerges is in a $\lambda\phi^4$ model. For simplicity, let us consider ϕ to be a real scalar field in one (spatial) dimension, *i.e.* a static field,

$$\mathcal{L}(\phi(x), \partial_x\phi(x)) = -\frac{1}{2}\left(\frac{d\phi}{dx}\right)^2 - V(\phi), \quad V(\phi) = \frac{\lambda}{4}(\phi^2 - \eta^2)^2, \quad \lambda, \eta^2 > 0. \tag{1.8}$$

The interaction term in eq. (1.8) is known as the *double well* potential. It corresponds to a cut with the plane where $\mathrm{Re}(\phi) = 0$ to the potential shown in Figure 1.1. It has two classical ground states at $\phi = \pm\eta$. The field equation is

$$-\frac{d^2\phi}{dx^2} + \lambda(\phi^2 - \eta^2)\phi = 0. \tag{1.9}$$

Its solution, with the boundary conditions $d\phi/dx = 0$ at $x = \pm\infty$ and $\phi(\pm\infty) = \pm\eta$ (minimum energy states at $x = \pm\infty$), is

$$\phi(x) = \eta \tanh\left(\sqrt{\frac{\lambda}{2}}\eta x\right). \tag{1.10}$$

There is a region of width defined as $2\sqrt{2}/(\eta\sqrt{\lambda})$ that interpolates both asymptotic values of ϕ, see Figure 1.3. Most of the non-trivial energy is localized in this zone.

This kind of solutions are known as domain walls[1]: they consist of low-energy domains, separated by highly energetic walls. In this example, the reflection symmetry $\phi \to -\phi$ is broken in each asymptotic regime. In $d > 1$, the emergence of domain walls is often related to the spontaneous breaking of a discrete symmetry. As it was pointed out in Ref. [11], the existence of domain walls in the universe would introduce strong deviations of the homogeneity and isotropy of the Cosmic Microwave Background (CMB), which are not observed. Thus, this type of topological defects is not generally expected in the cosmos.

1.2.2 Monopoles

Monopoles were found as solutions to the equations of motion of non-Abelian gauge theories by Polyakov and 't Hooft [12, 13]. In this section we show an example, introduced by

[1] Being more precise, the usual name in one dimension is "kink". Its generalization to higher dimensions is known as "domain wall".

't Hooft in 1974 [13], of a non-Abelian gauge theory that has magnetic monopoles in four dimensions. The Lagrangian consists of a three-component real scalar field with a quartic interaction and a local symmetry group[2] SO(3)

$$\mathcal{L} = \frac{1}{2} D_\mu \phi^a D^\mu \phi^a - \frac{m^2}{2} \phi^a \phi^a - \frac{\lambda}{8} (\phi^a \phi^a)^2 - \frac{1}{4} G^a_{\mu\nu} G^{\mu\nu a}, \quad a = 1, 2, 3, \tag{1.11}$$

where $\lambda > 0$ and

$$\begin{aligned} G^a_{\mu\nu} &= \partial_\mu W^a_\nu - \partial_\nu W^a_\mu + g \epsilon^{abc} W^b_\mu W^c_\nu, \\ D_\mu \phi^a &= \partial_\mu \phi^a + g \epsilon^{abc} W^b_\mu \phi^c, \end{aligned} \tag{1.12}$$

where g is the gauge coupling and W^a_μ the gauge field. If one chooses $m^2 < 0$, the SO(3) gauge symmetry "breaks" and the potential has a form similar to the one shown in Figure 1.1. The minimum is found when

$$F^2 \equiv \phi^a \phi^a = |\phi|^2, \quad F^2 = -\frac{2m^2}{\lambda}. \tag{1.13}$$

In the broken phase, if one expands in the vicinity of a minimum, *e.g.*

$$\phi^1 = \phi^2 = 0, \; \phi^3 = F + h(x), \tag{1.14}$$

the fields W^1_μ and W^2_μ acquire a mass $M_W = gF$, while the third component of the field gets a mass $M_h = \sqrt{\lambda} F$. This third component that is left has an SO(2) symmetry that persists after the breaking of SO(3). In the Standard Model formulation, where instead of SO(3) we have SU(2), the combination $W^\pm = (W^1_\mu \pm i W^2_\mu)/\sqrt{2}$ would be identified with the $W^\pm$ bosons and the ϕ^3 component with the Higgs boson.

In order to find monopoles, 't Hooft proposed to seek spherically-symmetric and static solutions. In particular, he showed that if the fields have the following asymptotic behavior

$$\phi^a(\vec{r}) \sim F \frac{r^a}{r} \quad \text{when } r = |(r_1, r_2, r_3)| \to \infty \tag{1.15}$$

and the gauge is fixed as

$$W^a_i(\vec{r}) \sim -\epsilon_{iab} \frac{r^b}{g r^2}, \quad W^a_0(\vec{r}) = 0, \quad i = 1, 2, 3 \tag{1.16}$$

the field equations are satisfied and monopoles appear. For instance, the equation for ϕ is

$$\left(m^2 + \frac{\lambda}{2} \phi^b \phi^b \right) \phi^a = D^\mu D_\mu \phi^a. \tag{1.17}$$

By inserting the asymptotic expressions of eqs. (1.15) and (1.16), one sees that the left-hand side of eq. (1.17) is zero, while for the right-hand side we have

$$D_\mu \phi_a = \partial_\mu \left(\frac{F r_a}{r} \right) + F \epsilon_{abc} W^b_\mu \frac{r_c}{r}. \tag{1.18}$$

For $\mu = 0$ we readily see that this expression is zero, if the gauge is fixed as in eq. (1.16). For the spatial components we derive the first term

$$D_i \phi_a = F \left(\frac{\delta_{ia}}{r} - \frac{r_i r_a}{r^3} \right) - F \epsilon_{abc} \epsilon_{ibd} \frac{r_c r_d}{r^3}. \tag{1.19}$$

[2]For the group index a, the upper or lower position does not matter.

We use the identity $\epsilon_{abc}\epsilon_{ibd} = \delta_{ia}\delta_{cd} - \delta_{ad}\delta_{ci}$ to obtain

$$D_i\phi_a = F\left[\frac{\delta_{ia}}{r} - \frac{r_i r_a}{r^3} - \frac{\delta_{ia}}{r} + \frac{r_i r_a}{r^3}\right] = 0. \tag{1.20}$$

To find the monopoles, one introduces a tensor $F_{\mu\nu}$ generalizing the usual electromagnetic tensor. 't Hooft proposes

$$F_{\mu\nu} = \frac{1}{|\phi|}\phi^a G^a_{\mu\nu} - \frac{1}{g|\phi|^3}\epsilon^{abc}\phi^a D_\mu\phi^b D_\nu\phi^c, \tag{1.21}$$

because if one inserts the expression at the minimum $\phi^1 = \phi^2 = 0$, $\phi^3 = F$, the usual version of $F_{\mu\nu} = \partial_\mu W^3_\nu - \partial_\nu W^3_\mu$ is recovered. The asymptotic expressions (1.15) and (1.16) imply that the second term of eq. (1.21) vanishes at $r \to \infty$. For the first term we compute

$$\phi_a G^a_{\mu\nu} = -\frac{F r^a}{r}\left[\partial_\mu W^a_\nu - \partial_\nu W^a_\mu + g\epsilon^{abc}W^b_\mu W^c_\nu\right]. \tag{1.22}$$

Again, if $\mu = 0$ or $\nu = 0$ the equation is zero due to the gauge fixing in eq. (1.16). Thus, we consider only the spatial components

$$\begin{aligned}
\phi_a G^a_{ij} &= -\frac{F r_a}{gr}\left[\partial_i\left(\frac{\epsilon_{jab}r_b}{r^2}\right) - \partial_j\left(\frac{\epsilon_{iab}r_b}{r^2}\right) - \frac{1}{r^4}\epsilon_{abc}\epsilon_{ibd}\epsilon_{jcf}r_d r_f\right] \\
&= -\frac{F r_a}{gr}\left[\frac{\epsilon_{jab}}{r^4}(\delta_{bi}r^2 - 2r_i r_b) - \frac{\epsilon_{iab}}{r^4}(\delta_{jb}r^2 - 2r_j r_b) - \frac{1}{r^4}\epsilon_{abc}\epsilon_{ibd}\epsilon_{jcf}r_d r_f\right] \\
&= -\frac{F r_a}{gr^5}\left[r^2(\epsilon_{jai} - \epsilon_{iaj}) + 2(r_j r_b\epsilon_{iab} - r_i r_b\epsilon_{jab}) - \epsilon_{abc}\epsilon_{ibd}\epsilon_{jcf}r_d r_f\right].
\end{aligned} \tag{1.23}$$

Since $r_a r_b \epsilon_{jab}$ is the product of a symmetric tensor with an antisymmetric one, the term vanishes. One may also show that

$$r_a\epsilon_{abc}\epsilon_{ibd}\epsilon_{jcf}r_d r_f = r^2 r_a\epsilon_{ija}, \tag{1.24}$$

by using the identity above eq. (1.20). Therefore

$$\phi_a G^a_{ij} = -\frac{F\epsilon_{ija}r_a}{gr^5}\left[r^2(\epsilon_{ija} + \epsilon_{ija}) - r^2\epsilon_{ija}\right] = -\frac{F}{gr^3}\epsilon_{ija}r_a, \tag{1.25}$$

which in turn yields

$$F_{0\mu} = 0, \quad F_{ij} = -\frac{1}{gr^3}\epsilon_{ija}r_a. \tag{1.26}$$

The magnetic field components correspond to

$$B_1 = -F_{23} = \frac{r_1}{gr^3}, \quad B_2 = F_{13} = \frac{r_2}{gr^3}, \quad B_3 = -F_{12} = \frac{r_3}{gr^3}. \tag{1.27}$$

Then

$$\vec{B} = \frac{\hat{r}}{gr^2}, \quad \hat{r} = \frac{\vec{r}}{r}. \tag{1.28}$$

Hence, we see that the model presented here indeed allows for magnetic monopoles with charge $g_M = 1/g$ as a solution. In Ref. [13], the monopole mass is estimated to be

$$M \simeq \frac{4\pi}{g^2}M_W \simeq 137 M_W, \tag{1.29}$$

where we assumed $g = e$ (electric charge) by analogy. If we insert the mass of the W boson $M_W \simeq 80$ GeV , although we are not dealing with the Standard Model, then a monopole

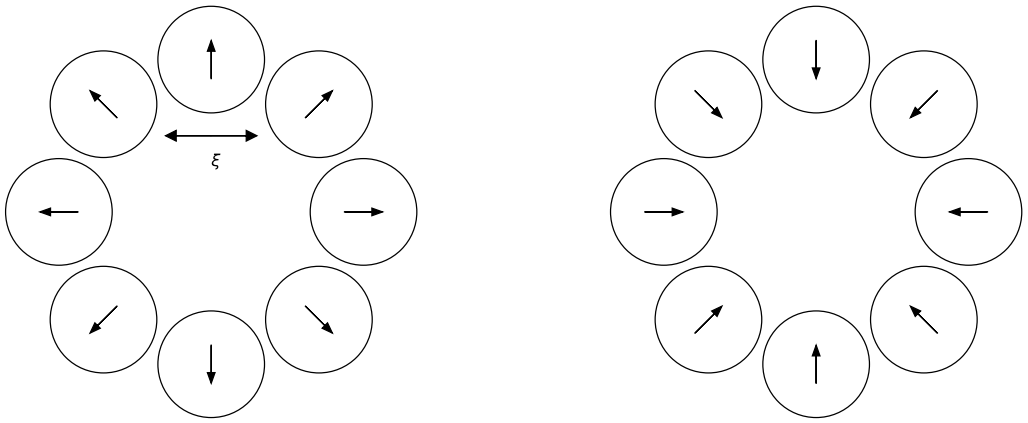

Figure 1.4: The left-hand diagram corresponds to a configuration where the minimum of the potential points radially outward for different domains, *i.e.* a monopole, as in eq. (1.15). The right-hand diagram represents an antimonopole.

would be highly massive, which makes these hypothetical particles very hard to produce in accelerators.

In the context of the Kibble mechanism, the monopoles form in the boundaries between the domains, see Figure 1.4. Since they are defects of dimension zero, we expect their density to be $1/\xi^3$, where ξ is the correlation length introduced in eq. (1.4). Monopoles appear in Grand Unified Theories (GUTs) as well (for instance in SU(5) [14] and SO(10) [15]), but their mass estimate is about 10^{16} GeV and the density of defects in the universe is unrealistically large, as discussed in Ref. [16].

1.2.3 Cosmic strings

To finish this section, we discuss cosmic strings. The simplest model where *local* cosmic strings appear is the Abelian Higgs model, *i.e.* a one-component complex scalar field, $\phi(x) \in \mathbb{C}$, with a U(1) gauge symmetry, described by the Lagrangian

$$\mathcal{L} = (D_\mu \phi)^\dagger D^\mu \phi - \lambda \left(\phi^\dagger \phi - \frac{\eta^2}{2} \right)^2 - \frac{1}{4} F_{\mu\nu} F^{\mu\nu}, \tag{1.30}$$

where

$$\begin{aligned} F_{\mu\nu} &= \partial_\mu A_\nu - \partial_\nu A_\mu, \\ D_\mu \phi &= \partial_\mu \phi + ieA_\mu \phi. \end{aligned} \tag{1.31}$$

The potential corresponds to Figure 1.1. Once again, a ground state is found when

$$\langle \phi \rangle = \frac{\eta}{\sqrt{2}} e^{i\theta}, \quad \theta \in [0, 2\pi). \tag{1.32}$$

As we have mentioned before, the value of θ can be different in non-causally connected regions. If one traces a closed loop around several domains, the phase of the ground state could change by a factor of $2n\pi$, with $n \in \mathbb{Z}$, see Figure 1.5. In the case when $n \neq 0$, we say that a *cosmic string* passes through the loop. This would correspond to tracing a closed loop around the circle of minima in the potential. The core of the string corresponds to the center of the potential, where $\phi = 0$.

In 1973 Nielsen and Olesen [17] found, in a more quantitative manner, cosmic strings in this model. Their idea is to search for static cylindrically-symmetric solutions of the

form

$$\phi(\vec{r}) = \frac{\eta}{\sqrt{2}} e^{in\theta} f(r), \quad A_i(\vec{r}) = -\epsilon_{ij} x^j \frac{n}{er^2} g(r), \quad i,j = 1,2, \quad n \in \mathbb{Z}, \tag{1.33}$$

where r and θ are the polar coordinates. The asymptotic behavior of $f(r)$ and $g(r)$ is proposed to be

$$\lim_{r\to\infty} f(r) = 1, \quad \lim_{r\to\infty} g(r) = 1, \tag{1.34}$$

and $f(0) = g(0) = 0$. By plugging the Ansätze (1.33) in the equations of motion,

$$\begin{aligned} \left[D_\mu D^\mu + 2\lambda \left(|\phi|^2 - \frac{1}{2}\eta^2 \right) \right] \phi &= 0, \\ \partial_\nu F^{\mu\nu} + ie(\phi^\dagger D^\mu \phi - \phi D^\mu \phi^\dagger) &= 0, \end{aligned} \tag{1.35}$$

one can find approximate solutions for $f(r)$ and $g(r)$, as shown in Refs. [17,18]. Now, if we compute the magnetic flux through a closed loop in the plane $z = 0$ for r approximating to infinity, we have

$$\int \vec{B} \cdot d\vec{s} = \int (\nabla \times \vec{A}) \cdot d\vec{s} = \oint_{S^1_\infty} \vec{A} \cdot d\vec{l} = \int_0^{2\pi} A_\theta \, r d\theta = \int_0^{2\pi} \frac{n}{er} \, r d\theta = \frac{2\pi n}{e}, \tag{1.36}$$

where S^1_∞ denotes a circle with radius approaching infinity. Thus, we see that the magnetic flux is quantized. In other words, there is a winding, given by the winding number n. In condensed matter, these solutions for the fields are known as flux tubes in superconductors. In particle physics, they are known as cosmic strings. It has been proved [17,18] that these strings have an energy density (energy per length, known as string tension) $\mu \propto \eta^2$. The value of η fixes the energy scale. For typical GUTs $\eta \simeq 10^{16}$ GeV, while for an electroweak phase transition $\eta \simeq 10^2$ GeV.

Until now, cosmic strings have not been observed. However, there is no evidence that discourages their existence, contrary to the case of monopoles and domain walls. Still, the string tension is constrained by the CMB data and simulations. For instance, Ref. [19] provides an upper bound of $\mu < 1.584 \times 10^{31}$ GeV^2, which hardly allows for GUT strings, if we assume that their tension is proportional to η^2. At some stage it was believed that cosmic strings could be the *seeds* for the formation of large structures, such as galaxies. This point of view is now discarded by COBE and WMAP data for the Cosmic Microwave Background [20–23]. One concludes that the CMB anisotropies cannot be explained through defect models. In particular, the acoustic peaks of the CMB are not predicted by any of these. Instead, their positions and shapes are more in agreement with the theory of inflation. These fluctuations in the CMB eventually lead to the formation of galaxies.

At last, we mention that it is also possible to find string solutions if the U(1) symmetry is global. In that case, however, their tension diverges.

More complete reviews of topological defects in the early universe can be found in Refs. [24–26].

In this thesis we will focus on the study of cosmic strings through their condensed matter analogue: vortex lines. To do so, we refer to the XY model, which we introduce in Chapter 2.

1.3 Zurek's contribution to the Kibble mechanism

In 1985, Zurek [3] complemented the Kibble mechanism by giving an estimate for the number of topological defects that remains after a second order phase transition, crossing

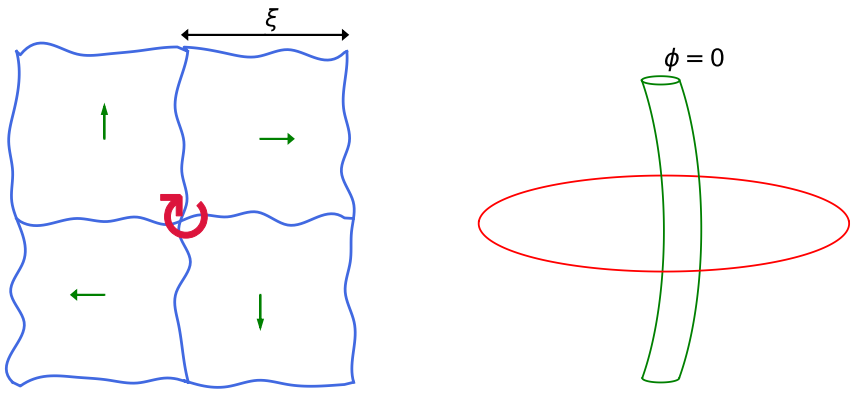

Figure 1.5: The left-hand diagram shows a configuration of domains where the ground state has different directions. If one traces a loop around the domains, the phase changes by 2π. The right-hand diagram depicts a cosmic string passing through the loop.

from the disordered phase to the ordered one. He did so for condensed matter systems, but the result is supposed to be valid for any setting where a second order phase transition arises. For that reason, the Kibble mechanism is nowadays sometimes known as the *Kibble-Zurek mechanism*. To explain the idea, let us suppose that we have a system with a critical temperature T_c. In equilibrium, close to criticality, the correlation length and the relaxation time (the time that the system takes to achieve equilibrium) behave as

$$\xi(\epsilon) = \frac{C_\xi}{|\epsilon|^\nu}, \quad \tau(\epsilon) = \frac{C_\tau}{|\epsilon|^{z\nu}}, \quad \epsilon = \frac{T_c - T}{T_c}, \tag{1.37}$$

where C_ξ and C_τ are constants. The exponent ν is a *critical exponent*, which depends on the *universality class* of the system, whereas z is known as the *dynamical critical exponent*. They can be obtained by simulations or experiments. The correlation length is determined, as we pointed out in eq. (1.4), through the decay of a correlation function.

We assume the system to be linearly quenched[3] with time

$$\epsilon(t) = \frac{t}{\tau_Q} \quad \text{or} \quad T(t) = T_c\left(1 - \frac{t}{\tau_Q}\right) \quad t \in [-\tau_Q, \tau_Q], \tag{1.38}$$

where τ_Q is known as the *inverse cooling rate*. This parameter controls the speed of the cooling process. Note that we have the following values of T at $t = -\tau_Q, 0$ and τ_Q

$$T(t) = \begin{cases} T = 2T_c & \text{at } t = -\tau_Q, \\ T = T_c & \text{at } t = 0, \\ T = 0 & \text{at } t = \tau_Q. \end{cases} \tag{1.39}$$

If we choose a large enough τ_Q, the system will remain in equilibrium during each instant of time of the quenching, *i.e.* the process will be adiabatic. However, since the relaxation time diverges at T_c, the rate at which $\epsilon(t)$ evolves ($|\epsilon/\dot{\epsilon}| = t$) will be below τ, temporarily taking the system out of equilibrium. Then, we say that the system is in a frozen stage. If one keeps cooling the system, the relaxation time lowers and the system leaves the frozen stage. This process is illustrated in Figure 1.6.

The main predictions that Zurek made are the behavior of the correlation length and the density of topological defects at the transition between the adiabatic and frozen stages.

[3]In the literature, the term *quench* is used as synonym of cooling in this context.

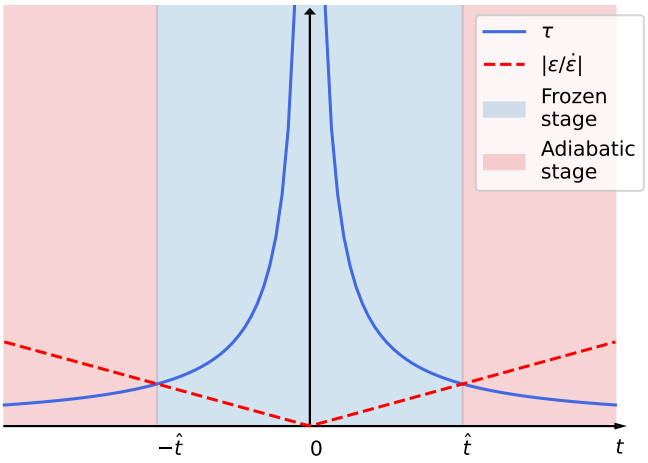

Figure 1.6: We linearly cool the system with time, starting at equilibrium at $T = 2T_c$, down to $T = 0$. Before $-\hat{t}$, the evolution rate of ϵ, $|\epsilon/\dot{\epsilon}|$, is above τ. Then, if one quenches the system very slowly, it remains in equilibrium for $t < -\hat{t}$ (adiabatic stage). In the interval bounded by $-\hat{t}$ and $\hat{t}$, the relaxation time grows larger than the dashed line. Therefore, it is impossible for the system to achieve equilibrium (frozen stage). For $t > \hat{t}$ the equilibrium can be recovered, since τ decreases.

We denote the time at which this transition is reached as $\pm\hat{t}$. Such predictions can be easily deduced by equating the relaxation time with the evolution rate of $\epsilon(t)$

$$\tau(\hat{t}\,) = \frac{C_\tau}{|\epsilon(\hat{t}\,)|^{z\nu}} = \left|\frac{\epsilon(\hat{t}\,)}{\dot{\epsilon}(\hat{t}\,)}\right| = \hat{t}, \quad \epsilon(\hat{t}\,) = \frac{\hat{t}}{\tau_Q} \quad \Longrightarrow \quad \hat{t} = (C_\tau \tau_Q^{z\nu})^{\frac{1}{1+z\nu}}. \tag{1.40}$$

Then we substitute in ϵ

$$\hat{\epsilon} \equiv \epsilon(\hat{t}\,) = \left(\frac{C_\tau}{\tau_Q}\right)^{\frac{1}{1+z\nu}}. \tag{1.41}$$

Therefore, the correlation length is given by

$$\hat{\xi} \equiv \xi(\hat{t}\,) = C_\xi \left(\frac{\tau_Q}{C_\tau}\right)^{\frac{\nu}{1+z\nu}}. \tag{1.42}$$

The density of topological defects is obtained if we assume that they have dimension D and the system dimension d

$$n \sim \frac{\hat{\xi}^D}{\hat{\xi}^d} \propto \left(\frac{1}{\tau_Q}\right)^{\frac{(d-D)\nu}{1+z\nu}}. \tag{1.43}$$

For cosmic strings (one dimensional objects) in three spatial dimensions we have $d-D = 2$, the exponents z and ν will be discussed later in the thesis.

We remark that eq. (1.43) is only valid when the relaxation time follows a power-law, as a function of $|\epsilon|$, in the vicinity of the critical point. This is the case of many models, like the one that we will study here.

A more complete review of Zurek's contributions, together with an extension of his prediction for quantum systems, is given in Ref. [27]. Several experiments have tried to test his prediction, eq. (1.43), in condensed matter systems [28]. Some of them successfully verified the power-law dependence of the density of topological defects on the inverse cooling rate. For instance, in Ref. [4] the authors considered a two-dimensional optical system: a liquid crystal light valve illuminated by a uniform laser beam. In this case,

a diffraction pattern appears and there is a phase transition controlled by the laser's intensity. The topological defects are identified as points in the pattern. A power-law $n \propto \tau_Q^{-1/2}$ is predicted by eq. (1.43), if one uses the corresponding critical exponents for this particular system. Ref. [4] obtains a very close value, -0.50 ± 0.04, for the exponent.

Other experiments only confirm Zurek's prediction partially, *i.e.* a power-law is observed but the scaling exponent is different. Ref. [5] presents an experiment of a fluid undergoing a conduction-convection transition, controlled by the temperature. The density of topological defects is observed to be proportional to $\tau_Q^{-0.27}$. For this system, the critical exponents and eq. (1.43) predict $\tau_Q^{-1/2}$. Thus we see a discrepancy.

In this work we will compute the density of topological defects of the 3d XY model after a quenching process in order to test eq. (1.43). Our tool are Monte Carlo simulations, which we describe in Chapter 3.

Chapter 2

The XY model

The XY model is a classical spin model defined by the Hamiltonian

$$H = -J \sum_{\langle ij \rangle} \vec{S}_i \cdot \vec{S}_j = -J \sum_{\langle ij \rangle} \cos(\theta_i - \theta_j), \quad \vec{S}_i = (\cos\theta_i, \sin\theta_i) \in \mathbb{S}^1, \quad \theta_i \in (-\pi, \pi], \tag{2.1}$$

where $J > 0$ is a coupling constant and the sum runs over the nearest neighbors on a lattice with N sites. In this thesis we assume periodic boundary conditions. We see that the Hamiltonian is invariant under global O(2) transformations (planar rotations). For that reason, the system described by eq. (2.1) is also known as the O(2) model. It is used as a *toy model* to study numerical methods, topology or phase transitions. Still, it is known that it describes some real systems with good precision, such as superfluid ^{4}He [29–32].

Of particular interest is the two-dimensional version, because of the Berezinskiĭ – Kosterlitz–Thouless (BKT) transition [33–35]. This is a *topological phase transition*, caused by the topological defects (vortices in this case) of the system. Unlike a usual continuous transition, the BKT transition is not related to the breaking of a symmetry. Therefore, it is not in contradiction with the *Mermin–Wagner theorem* [36], which states that a continuous, global symmetry cannot be spontaneously broken in two dimensions. Kosterlitz and Thouless were awarded with the Nobel Prize in 2016 due to the explanation of the BKT transition [37, 38].

In three dimensions, the topological defects are known as *vortex lines* (lines that pass through a set of vortices), which are one-dimensional objects. They can be connected to form large networks throughout the lattice and be interpreted as cosmic strings.

In this chapter, we will review the important features of the two- and three-dimensional version of the XY model.

2.1 Correlation function

In order to motivate the existence of a phase transition in two dimensions, we begin by analyzing the behavior of the correlation function at low temperature T. We will do so for general dimension $d \geq 2$. At low T, the system is dominated by configurations with small angles between nearest neighbor spins and we can expand the cosine up to second order in the Hamiltonian

$$\beta H \approx -\beta J d N + \frac{\beta J}{2} \sum_{\langle ij \rangle} (\theta_i - \theta_j)^2, \quad \beta \equiv \frac{1}{T}. \tag{2.2}$$

If we consider that the lattice sites are separated by a distance a, we can rewrite the second term as

$$\frac{J\beta}{2}\sum_{\langle ij\rangle}(\theta_i-\theta_j)^2=\frac{J\beta}{2}\sum_{\vec{r},\mu}\left(\theta(\vec{r}+a\vec{e}_\mu)-\theta(\vec{r})\right)^2,\quad \mu=1,2\cdots d, \tag{2.3}$$

where $\vec{r}$ denotes the position vector and $\vec{e}_\mu$ the unit vector in the μ-direction. If a is small enough, we can approximate the sum by an integral and the angle difference by a derivative

$$\beta H\approx\beta E_0+\frac{\beta J a^{2-d}}{2}\int d^dr\,|\nabla\theta(\vec{r})|^2, \tag{2.4}$$

where $E_0=JdN$ is the ground state energy. We extend the range of θ to $(-\infty,\infty)$ and define the *spin stiffness* as $\rho_s=Ja^{2-d}$. Then, the partition function takes the form[1]

$$Z=\int\mathcal{D}\theta\,e^{-\beta H}\approx\int\mathcal{D}\theta\,\exp\left(-\beta E_0-\frac{\beta\rho_s}{2}\int d^dr\,|\nabla\theta(\vec{r})|^2\right). \tag{2.5}$$

Now, let us compute the spin correlation function

$$\begin{aligned}\langle\vec{S}(\vec{x})\cdot\vec{S}(\vec{0})\rangle&=\left\langle\cos\Big(\theta(\vec{x})-\theta(\vec{0})\Big)\right\rangle=\mathrm{Re}\left\langle e^{i\left(\theta(\vec{x})-\theta(\vec{0})\right)}\right\rangle\\&=\mathrm{Re}\left[\frac{1}{Z}\int\mathcal{D}\theta\exp\Big(-\beta E_0-\frac{\beta\rho_s}{2}\int d^dr\,|\nabla\theta(\vec{r})|^2+i(\theta(\vec{x})-\theta(\vec{0}))\Big)\right].\end{aligned} \tag{2.6}$$

We analyze the exponent

$$I(\vec{x})\equiv-\frac{\beta\rho_s}{2}\int d^dr\,|\nabla\theta(\vec{r})|^2+i(\theta(\vec{x})-\theta(\vec{0})) \tag{2.7}$$

under a Fourier transformation[2]

$$\theta(\vec{x})=\frac{1}{(2\pi)^d}\int d^dk\,\theta(\vec{k})e^{-i\vec{k}\cdot\vec{x}},\quad \nabla\theta(\vec{x})=-\frac{i}{(2\pi)^d}\int d^dk\,\theta(\vec{k})e^{-i\vec{k}\cdot\vec{x}}\,\vec{k}. \tag{2.8}$$

The latter implies that

$$\begin{aligned}\int d^dr\,|\nabla\theta(\vec{r})|^2&=-\frac{1}{(2\pi)^{2d}}\int d^dr\,d^dk\,d^dk'\,\theta(\vec{k})\theta(\vec{k}')\vec{k}\cdot\vec{k}'e^{i\vec{r}\cdot(\vec{k}+\vec{k}')}\\&=\frac{1}{(2\pi)^d}\int d^dk\,k^2\theta(\vec{k})\theta(-\vec{k}),\end{aligned} \tag{2.9}$$

where we used

$$\int d^dr\,e^{i\vec{r}\cdot(\vec{k}+\vec{k}')}=(2\pi)^d\delta(\vec{k}+\vec{k}'). \tag{2.10}$$

Thus,

$$I(\vec{x})=\frac{1}{(2\pi)^d}\int d^dk\,\left[-\frac{\beta\rho_s}{2}k^2\theta(\vec{k})\theta(-\vec{k})+i(e^{-i\vec{k}\cdot\vec{x}}-1)\theta(\vec{k})\right]. \tag{2.11}$$

For convenience we rewrite eq. (2.11) in the following way, by completing the square

$$\begin{aligned}I(\vec{x})=&-\frac{1}{(2\pi)^d}\int d^dk\,\frac{\beta\rho_s}{2}k^2\left[\theta(-\vec{k})-i\left(e^{-i\vec{k}\cdot\vec{x}}-1\right)\frac{1}{\beta\rho_s k^2}\right]\\&\times\left[\theta(\vec{k})-i\left(e^{i\vec{k}\cdot\vec{x}}-1\right)\frac{1}{\beta\rho_s k^2}\right]\\&-\frac{1}{(2\pi)^d}\int d^dk\,\frac{1}{2\beta\rho_s k^2}\left(e^{i\vec{k}\cdot\vec{x}}-1\right)\left(e^{-i\vec{k}\cdot\vec{x}}-1\right),\end{aligned} \tag{2.12}$$

[1] We work in units of $k_B=1$.

[2] We denote $\theta(\vec{x})$ and its Fourier transformation $\theta(\vec{k})$ with the same symbol.

where we have used

$$\int d^d k e^{i\vec{k}\cdot\vec{x}} = \int d^d k e^{-i\vec{k}\cdot\vec{x}}. \tag{2.13}$$

The reason to do this is that now we have split the integral in two parts: one that depends on θ and another one that does not include it. We can perform a change of variables

$$\begin{aligned} \theta^*(\vec{k}\,) &= \theta(-\vec{k}\,) = \theta'(-\vec{k}\,) + i\left(e^{-i\vec{k}\cdot\vec{x}} - 1\right)\frac{1}{\beta\rho_s k^2}, \\ \theta(\vec{k}\,) &= \theta'(\vec{k}\,) + i\left(e^{i\vec{k}\cdot\vec{x}} - 1\right)\frac{1}{\beta\rho_s k^2}, \end{aligned} \tag{2.14}$$

to obtain

$$\begin{aligned} I(\vec{x}\,) = &-\frac{1}{(2\pi)^d}\int d^d k\,\frac{\beta\rho_s}{2}k^2\theta'(-\vec{k}\,)\theta'(\vec{k}\,) \\ &-\frac{1}{(2\pi)^d}\int d^d k\,\frac{1}{2\beta\rho_s k^2}\left(e^{i\vec{k}\cdot\vec{x}} - 1\right)\left(e^{-i\vec{k}\cdot\vec{x}} - 1\right), \end{aligned} \tag{2.15}$$

where we used

$$\int d^d k \frac{1}{k^2} e^{i\vec{k}\cdot\vec{x}} = \int d^d k \frac{1}{k^2} e^{-i\vec{k}\cdot\vec{x}}. \tag{2.16}$$

Since the transformations (2.14) are shifts, the functional measure $\mathcal{D}\theta$ does not change. Then, if we insert eqs. (2.5) and (2.15) into eq. (2.6) we obtain

$$\begin{aligned} \langle \vec{S}(\vec{x}\,)\cdot\vec{S}(\vec{0}\,)\rangle &= \exp\left[-\frac{1}{(2\pi)^d}\int d^d k\,\frac{1}{2\beta\rho_s k^2}\left(e^{i\vec{k}\cdot\vec{x}} - 1\right)\left(e^{-i\vec{k}\cdot\vec{x}} - 1\right)\right] \\ &= \exp\left[-\frac{1}{(2\pi)^d}\frac{1}{\beta\rho_s}\int d^d k\,\frac{1 - e^{-i\vec{k}\cdot\vec{x}}}{k^2}\right] \\ &\equiv \exp\left(-g(\vec{x})\right). \end{aligned} \tag{2.17}$$

The solution to the integral yields the low-temperature behavior of the correlation function. We will compute its asymptotic form for $d \geq 2$. We distinguish two cases:

- For $d > 2$ and $x = |\vec{x}|$ we have

$$\begin{aligned} g(\vec{x}) &= \frac{1}{(2\pi)^d}\frac{1}{\beta\rho_s}\int d^d k\,\frac{1}{k^2} - \frac{1}{(2\pi)^d}\frac{1}{\beta\rho_s}\int d\Omega_d \int_0^\infty dk\, k^{d-1}\frac{e^{-ikx\cos\theta}}{k^2} \\ &= \frac{1}{(2\pi)^d}\frac{1}{\beta\rho_s}\int d^d k\,\frac{1}{k^2} - \frac{1}{(2\pi)^d}\frac{1}{\beta\rho_s}\int d\Omega_d\,\frac{\Gamma(d-2)}{(ix\cos\theta)^{d-2}}, \end{aligned} \tag{2.18}$$

  where Ω_d is the solid angle in d dimensions. If we take the limit $x \to \infty$, the second term vanishes and we are left with

$$\begin{aligned} g &\sim \frac{1}{(2\pi)^d}\frac{1}{\beta\rho_s}\int d^d k\,\frac{1}{k^2} \\ &= \frac{1}{(2\pi)^d}\frac{1}{\beta\rho_s}\int d\Omega_d \int_0^\Lambda dk\, k^{d-3}. \end{aligned} \tag{2.19}$$

  Since the second integral diverges in infinity, we introduce a UV cut-off Λ. Therefore, for large x, we have

$$g \sim \frac{1}{(2\pi)^d}\frac{S_d}{\beta\rho_s(d-2)}\Lambda^{d-2}, \quad d > 2, \tag{2.20}$$

  where S_d is the surface of a d-dimensional sphere,

$$S_d = \frac{2\pi^{d/2}}{\Gamma\left(\frac{d}{2}\right)}. \tag{2.21}$$

- Now we consider the case $d = 2$. Again we introduce a UV cut-off

$$\begin{aligned} g(\vec{x}\,) &= \frac{1}{(2\pi)^2}\frac{1}{\beta\rho_s}\int d^2k\,\frac{1-e^{-ikx\cos\theta}}{k^2} \\ &= \frac{1}{(2\pi)^2}\frac{1}{\beta\rho_s}\int_0^\Lambda dk\int_0^{2\pi} d\theta\,\frac{1-e^{-ikx\cos\theta}}{k} \\ &= \frac{1}{2\pi}\frac{1}{\beta\rho_s}\int_0^\Lambda dk\,\frac{1-J_0(kx)}{k}, \end{aligned} \tag{2.22}$$

  where J_0 is the Bessel function of order zero. We perform the change of variable $q = kx$ and split the integral in the following way

$$\int_0^1 dq\,\frac{1-J_0(q)}{q} + \int_1^{\Lambda x} dq\,\frac{1-J_0(q)}{q}. \tag{2.23}$$

  The dominant part of this integral corresponds to

$$\int_1^{\Lambda x} dq\frac{1}{q} = \ln(\Lambda x). \tag{2.24}$$

  The other terms,

$$\int_0^1 dq\,\frac{1-J_0(q)}{q} - \int_1^{\Lambda x} dq\,\frac{J_0(q)}{q}, \tag{2.25}$$

  can be absorbed in a constant C (independent of x) if we let $\Lambda \to \infty$. Thus, g takes the form

$$g(\vec{x}\,) \sim \frac{1}{2\pi}\frac{1}{\beta\rho_s}\ln(\Lambda x) + C, \quad d = 2. \tag{2.26}$$

By using eqs. (2.20) and (2.26) we obtain

$$\langle \vec{S}(\vec{x}\,)\cdot\vec{S}(\vec{0}\,)\rangle \sim \begin{cases} \exp\left(-\frac{1}{(2\pi)^d}\frac{S_d\Lambda^{d-2}}{\rho_s(d-2)}T\right) & d > 2, \\ \\ A(\Lambda x)^{-\frac{T}{2\pi\rho_s}} & d = 2, \end{cases} \tag{2.27}$$

where $A = e^C$ is a dimensionless constant. We see that in dimensions larger than two, for large x the correlation function is asymptotically constant. Then, we say that there is a *long-range order*. For $d = 2$ there is an algebraic decay and the large x limit yields a vanishing correlation function at $T \neq 0$. This corresponds to a *quasi-long-range order*. We mention the fact that an algebraic decay usually occurs at the critical temperature T_c of a transition. For this particular model in two dimensions, we observe that the algebraic decay is always present at low temperature, which indicates a diverging correlation length.

On the other hand, for the high-temperature regime it is possible to show that (see for instance Ref. [39])

$$\langle \vec{S}(\vec{x}\,)\cdot\vec{S}(\vec{0}\,)\rangle = e^{-x/\xi}, \quad \xi = \frac{a}{\ln(2T/J)}. \tag{2.28}$$

This result does not depend on the dimension. Therefore there is always an exponential decay for high temperature. The different types of decay in the low- and high-temperature regime in two dimensions suggest that there could be a phase transition. However, it cannot be related to the spontaneous breaking of symmetry, otherwise there would be a contradiction with the Mermin-Wagner theorem.

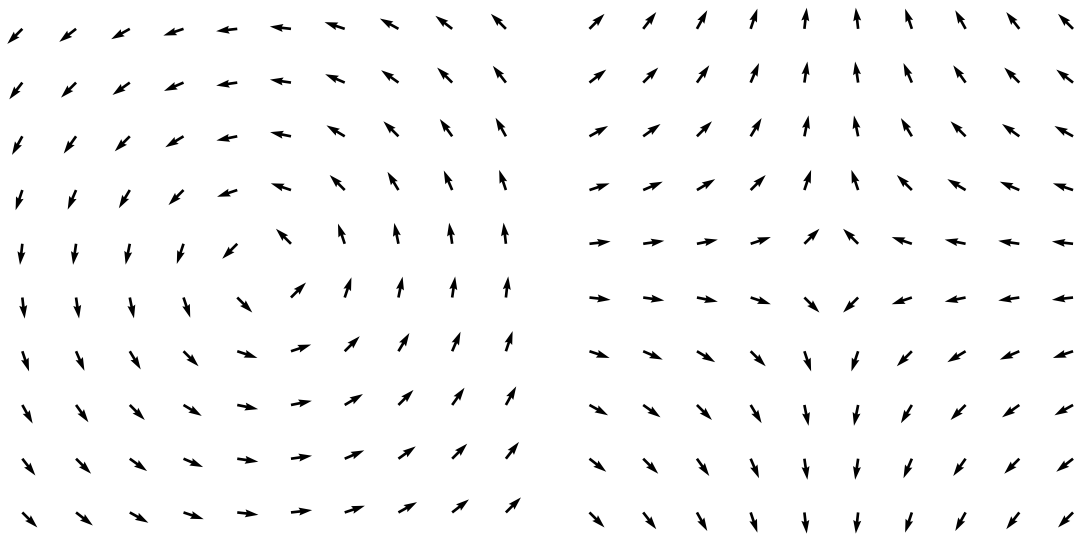

Figure 2.1: Vector field associated with a vortex for $n = 1$, $C = \pi/2$ (left-hand side) and an anti-vortex for $n = -1$, $C = \pi$ (right-hand side), see eq. (2.31).

2.2 Vortices in two dimensions

Berezinskiĭ [33,34] and later Kosterlitz and Thouless [35] explained this transition with the dynamics of the topological defects of the system, which correspond to vortices. To show that these defects arise as minimal energy excitations, let us consider the variation of the Hamiltonian for small a (lattice spacing)

$$\begin{aligned}\frac{\delta H}{\delta\theta(\vec{x})} &= \frac{J}{2}\frac{\delta}{\delta\theta(\vec{x}\,)}\int d^2r\,|\nabla\theta(\vec{r}\,)|^2 \\ &= \frac{J}{2}\frac{\delta}{\delta\theta(\vec{x}\,)}\left(\int d^2r\,\left[\nabla\cdot(\theta\nabla\theta)\right] - \int d^2r\,\theta\nabla^2\theta\right) = 0. \end{aligned} \tag{2.29}$$

Using Gauss's theorem, we observe that the first term vanishes, for the case of periodic boundaries. Thus, the solutions to

$$\nabla^2\theta = 0 \tag{2.30}$$

yield the minimum energy configurations. A simple solution corresponds to a constant value of θ, but there are other type of functions that satisfy Laplace's equation. They are of the form

$$\theta(\varphi) = n\varphi + C, \tag{2.31}$$

where φ is the polar angle, θ the spin angle, n an integer number due to the 2π periodicity and C a constant. A graphical depiction of these configurations is shown in Figure 2.1. A subset of a configuration with $n = 1$ has a vortex, while for $n = -1$ we say that it has an anti-vortex.

In discrete space, the vortices can be determined by dividing the lattice into *plaquettes*, which are arrangements of four sites, as shown in Figure 2.2. The vorticity of a plaquette is

$$v_i = \frac{1}{2\pi}\left(\Delta\theta_{i,i+\hat{x}} + \Delta\theta_{i+\hat{x},i+\hat{x}+\hat{y}} + \Delta\theta_{i+\hat{x}+\hat{y},i+\hat{y}} + \Delta\theta_{i+\hat{y},i}\right), \tag{2.32}$$

where i is a lattice site and $\Delta\theta_{i,j} \equiv (\theta_j - \theta_i) \bmod 2\pi \in (-\pi, \pi]$, i and j are two neighboring sites. It turns out that v_i can only take the values $1, 0$ or -1.[3] Again, $v_i = 1$ represents a vortex and $v_i = -1$ an anti-vortex.

[3] In principle $|v_i| = 2$ is also possible but its statistical probability vanishes.

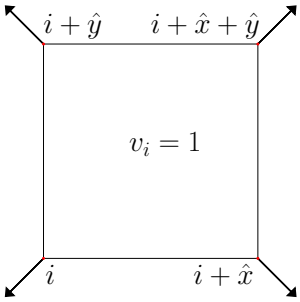

Figure 2.2: Plaquette on the lattice with vorticity $v_i = 1$.

For the moment we will work in the small a limit, *i.e.* with expression (2.31). The energy needed to create one of these configurations is

$$E_V - E_0 = \frac{J}{2}\int d^2r\,|\nabla\theta(\vec{r})|^2 = \frac{J}{2}\int_0^{2\pi}\int_{r_0}^{L}\frac{n^2}{r^2}rdrd\varphi = n^2\pi J\ln\frac{L}{r_0}, \tag{2.33}$$

where L represents the *linear size* of the system and r_0 the radius of the vortex core, related to the lattice spacing a. Now we will compute the Helmholtz free energy $F = E - TS$. To do so, we need the entropy, S, which we can obtain through Boltzmann's formula. If we take into account that the number of ways to arrange a vortex of size r_0 in an area of L^2, with resolution r_0, is proportional to L^2/r_0^2, then

$$S = \ln\left(A\frac{L^2}{r_0^2}\right), \tag{2.34}$$

where A is a constant. Hence

$$F = (n^2\pi J - 2T)\ln\frac{L}{r_0} + T\ln A. \tag{2.35}$$

For $T > n^2\pi J/2$ the first term of F is negative. Then, as L becomes larger, the free energy decreases. If $T < n^2\pi J/2$, when L grows the free energy increases. This indicates that for high temperature the density of vortices can be significant, because they become more stable configurations (the free energy is minimized). This again suggests the possibility of a phase transition. A rough estimate of the critical temperature is $T_c = \pi J/2$. The vortex proliferation is consistent with the decay of the correlation function for high temperatures, eq. (2.28). At $T > T_c$, the correlation $\langle\vec{S}(\vec{x})\cdot\vec{S}(\vec{0})\rangle$ decays exponentially, thus the spins are not very correlated over large distances. This implies that their orientations are mostly random, which in turn provides the possibility for the formation of a large number of vortices or anti-vortices. For low temperature, spins tend to align and the formation of vortices is suppressed.

Typical configurations have a number of defects, if the temperature is not too low and the volume not too small, thus one has to study the interaction between vortices and anti-vortices. Ref. [35] shows that the interaction energy between them is

$$E_{\text{int}} = -\pi J\sum_{i\neq j} n_i n_j \ln\frac{|\vec{r}_i - \vec{r}_j|}{r_0}, \tag{2.36}$$

where n_i is the vorticity of a defect. For a vortex–anti-vortex pair we have $n_i n_j < -1$ and the energy is minimized when they are bound together. If the distance between them goes to zero, the pair annihilates, yielding a net vorticity of $n = 0$. Moreover, from eq. (2.36) we

observe that the vortex–anti-vortex interaction is attractive ($\vec{F} = -\nabla E_{\text{int}}$), while defects with the same value of n interact via a repulsive force.

In order to derive eq. (2.36), it is necessary that

$$\sum_i n_i = 0. \tag{2.37}$$

With periodic boundaries this condition is actually implied by Stokes' theorem. This is consistent, since in Ref. [35] the authors point out that the total vorticity of the system has to be zero so that there can be a finite interaction energy between the vortices in an infinite volume. This can be seen if we take into account the energy needed to create a configuration with vortices,

$$E_V - E_0 = \left(\sum_i n_i\right)^2 \pi J \ln \frac{L}{r_0}. \tag{2.38}$$

For large L this diverges unless $\sum_i n_i = 0$.

When the distance between the members of a pair is large, their interaction force decreases. In such a case one can treat the vortices as if they were free. Thus, the BKT transition occurs between two phases. At low temperature, there is only a low density of tightly bound vortex–anti-vortex pairs. At high temperature the pairs unbind, giving rise to a significant density of free vortices.

2.3 3d XY model

In three dimensions, the XY model has a second order phase transition, which is not explained through topological defects. Still, it is possible to define the vorticity of each plaquette in the same way as in two dimensions, eq. (2.32). One difference is that now we have to consider each plaquette of the three-dimensional cubes that form the lattice. In addition, the cores of the vortices now form a one-dimensional line that crosses the plaquettes, see Figure 2.3. These lines can be connected by following a direction which is defined with the vorticity of the plaquettes, see Figure 2.4. The connections can extend throughout the lattice and form large loops and networks. For this reason, vortices in three dimensions are better known as *vortex lines* and are analogous to cosmic strings. Therefore one can use the 3d XY model as a testbed to study the dynamics of these defects in the universe and to test Zurek's prediction, explained in Section 1.3.

It has been conjectured that the properties of such networks could yield information about the phase transition in three dimensions [40, 41]. However, there is an ambiguity in the procedure to connect the lines that pass through each plaquette. Different ways to join them yield different strings properties. In Figure 2.5, we show an example where difficulties to connect the lines arise. Ref. [42] has explored this issue. In this work we will only study the dynamics of the lines that pass through each plaquette (without joining them), avoiding ambiguities with the manner to connect them to form large networks.

Since there is a second order phase transition, some thermodynamic quantities diverge in the infinite-volume limit at the critical temperature T_c, such as

$$C_V = \frac{\langle E^2\rangle - \langle E\rangle^2}{VT^2} \sim \frac{1}{|T - T_c|^\alpha}, \quad \text{Heat capacity,}$$

$$\chi_M = \frac{\langle M^2\rangle - \langle M\rangle^2}{V} \sim \frac{1}{|T - T_c|^\gamma}, \quad \text{Magnetic susceptibility,}$$

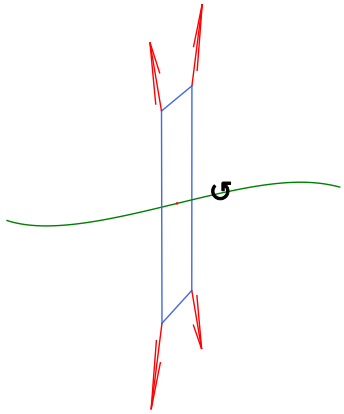

Figure 2.3: Vortex line passing through a plaquette with positive vorticity.

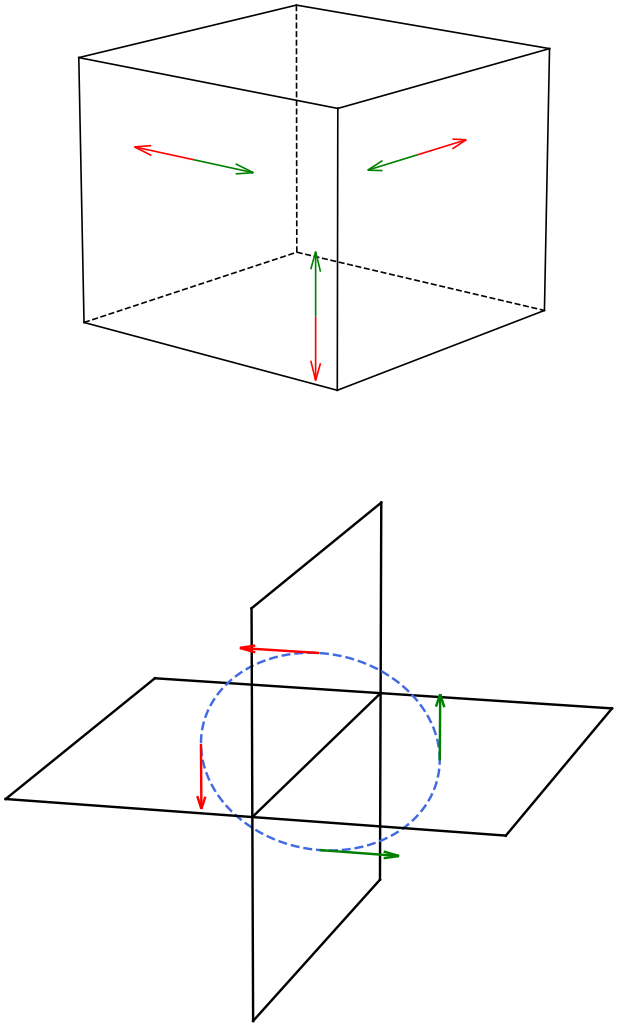

Figure 2.4: The upper panel shows a possible way to define the direction that a vortex line follows when passing through a plaquette. The green arrow indicates a vortex (pointing inwards the cube), while the red one refers to an anti-vortex (pointing outwards). The lower panel shows an example of a loop with definite direction crossing four plaquettes.

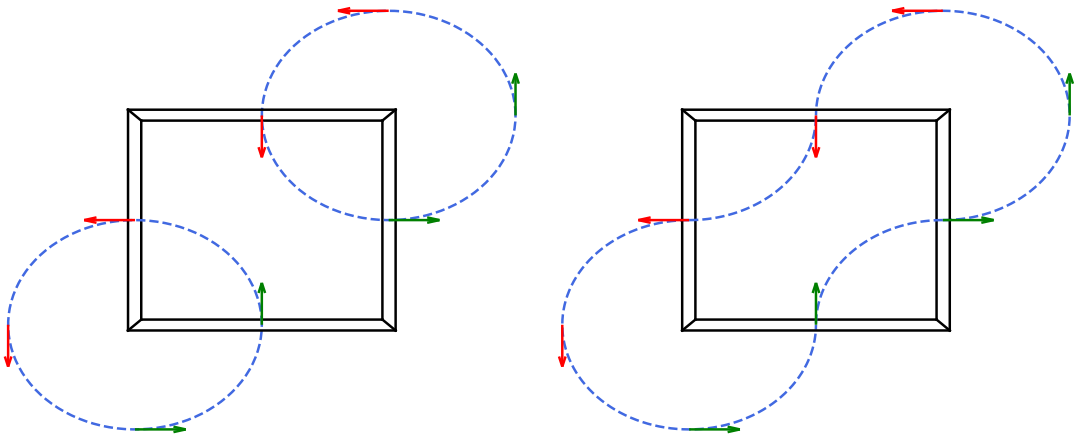

Figure 2.5: In some cubes of the lattice, there may be ambiguities on how to connect the vortex lines. For the example in this figure we see that there are two possible ways to connect them. Both manners yield different properties for the network [42].

$$\text{where} \quad M = |\vec{M}|, \quad \vec{M} = \sum_i \vec{S}_i, \quad \text{is the magnetization,}$$

$$\xi \sim \frac{1}{|T - T_c|^\nu}, \quad \text{Correlation length,} \tag{2.39}$$

where $\langle E \rangle$ is the energy expectation value, $\langle M \rangle$ the mean magnetization and V the volume.

The critical exponents and temperature can be obtained by means of Monte Carlo simulations. This has been reported many times with very high precision. Thus, we will not repeat those computations with our simulations. Instead, we only mention the value of the exponents and T_c, in units of $J = k_B = 1$, for future reference [43, 44]

$$\beta_c = \frac{1}{T_c} = 0.45416474(10), \quad \alpha = -0.0151(3), \quad \gamma = 1.3178(2), \quad \nu = 0.67169(7). \tag{2.40}$$

More complete reviews of the XY model, its topology and the BKT transition can be found in Refs. [38, 39, 45, 46].

Chapter 3

Monte Carlo simulations

In statistical mechanics one is usually interested in calculating expectation values

$$\langle \mathcal{O} \rangle = \frac{1}{Z} \operatorname{tr} \left(\mathcal{O} e^{-\beta \hat{H}} \right), \quad \beta = \frac{1}{T}, \tag{3.1}$$

where

$$Z = \operatorname{tr} \left(e^{-\beta \hat{H}} \right) \tag{3.2}$$

is the partition function of the system and $\hat{H}$ the Hamilton operator. In the functional integral formulation we can also write

$$\langle \mathcal{O} \rangle = \frac{1}{Z} \int \mathcal{D}[\sigma] \, \mathcal{O}[\sigma] e^{-\beta H[\sigma]}, \quad Z = \int \mathcal{D}[\sigma] \, e^{-\beta H[\sigma]}, \tag{3.3}$$

where the integral is over all the possible configurations. In field theory, the partition function is given by a functional integral in Euclidean space. In most cases, it is impossible to analytically compute $\langle \mathcal{O} \rangle$ for an arbitrary observable. Thus, numerical methods are often required to study statistical systems. The main objective of these methods is to generate a set of N configurations, $\{\sigma\}$, to numerically evaluate the functional integral as a sum over $\{\sigma\}$. Generating configurations that follow a uniform probability distribution is not useful, because some of them contribute much more to the partition function than others. The idea of *importance sampling* methods is to randomly generate configurations that are distributed according to the probability in equilibrium

$$p[\sigma] = \frac{1}{Z} e^{-\beta H[\sigma]}. \tag{3.4}$$

This can be achieved by Monte Carlo methods. That way, if $N \gg 1$, one can determine $\langle \mathcal{O} \rangle$ through

$$\langle \mathcal{O} \rangle \approx \frac{1}{N} \sum_{[\sigma]} \mathcal{O}\,[\sigma]\,. \tag{3.5}$$

Each evaluation of $\mathcal{O}$ for a given configuration $[\sigma]$ is called a *measurement*. The statistical error of eq. (3.5) decreases as $1/\sqrt{N}$. Many Monte Carlo methods rely on *Markov chains*. These are sequences of configurations where the creation of the n^{th} configuration only needs the information of the $(n-1)^{\text{th}}$ configuration. With long chains, one can obtain, in principle, the value of $\langle \mathcal{O} \rangle$ to an arbitrary precision. Still, one is limited to work with finite volumes in discrete space. In order to obtain the thermodynamic and continuum limits, the usual procedure is to work with high statistics (large N) for several volumes V (as large as possible) and lattice spacings a (as fine as possible) to extrapolate $\langle \mathcal{O} \rangle$ to $V \to \infty$ and $a \to 0$ with an educated guess.

In this chapter we will review the basic concepts of Markov chains needed to understand the working of Monte Carlo methods. Later, we will explain the implementation of four different algorithms (Metropolis, worm, cluster and heatbath algorithm). We refer to the XY model, although these algorithms are also applicable to other systems.

3.1 Markov chains

As we mentioned before, Markov chains are sequences of configurations where each new configuration is generated by considering only the previous one

$$[\sigma_0] \to [\sigma_1] \to [\sigma_2] \to \cdots \to [\sigma_{t-1}] \to [\sigma_t] \to \cdots . \tag{3.6}$$

The index t is known as the *Markov time*. The generation of a chain requires an initial configuration $[\sigma_0]$ and a transition probability that is independent of t, *i.e.*

$$T(\sigma' = \sigma_t | \sigma = \sigma_{t-1}) = T(\sigma'|\sigma), \tag{3.7}$$

where $T(\sigma'|\sigma)$ is the transition probability of moving from $[\sigma]$ to $[\sigma']$. This quantity has to be normalized

$$0 \leq T(\sigma'|\sigma) \leq 1, \quad \sum_{[\sigma']} T(\sigma'|\sigma) = 1. \tag{3.8}$$

The transition probability tells us how to update the configurations. It is important that the Markov chains that we generate in Monte Carlo simulations are *ergodic* or *irreducible*. This means that if we have two arbitrary configurations $[\sigma]$ and $[\sigma']$, the transition probability of moving from $[\sigma]$ to $[\sigma']$, after a finite number of updates, is larger than zero. If this property is not fulfilled, one could wrongly generate only a subset of the total sample space, see Figure 3.1. Furthermore, the ergodicity together with other conditions, such as

$$\sum_{[\sigma']} T(\sigma|\sigma') p[\sigma'] = p[\sigma] \quad \text{for all } [\sigma], \tag{3.9}$$

where $p[\sigma]$ is the *equilibrium distribution* or *stationary distribution*, ensure that in the limit $t \to \infty$ the probability distribution of the chain converges to, precisely, $p[\sigma]$. One can also guarantee that the large t limit will not be affected by our choice of $[\sigma_0]$. For a proof of these statements, see Ref. [47].

A sufficient condition to fulfill eq. (3.9) is

$$T(\sigma'|\sigma) p[\sigma] = T(\sigma|\sigma') p[\sigma'], \tag{3.10}$$

since the transition probability is normalized. This relation is known as *detailed balance*. It is important to remark that its solution is not unique for fixed $p[\sigma]$. There are different transition probabilities that agree with detailed balance. One can take advantage of this fact to invent efficient algorithms to perform simulations. In the following sections, we will briefly discuss some technical aspects related to Monte Carlo methods.

3.1.1 Autocorrelation

Before measuring any observable with the configurations generated through Monte Carlo algorithms, one has to perform a large number of updates to assure that our set $\{\sigma\}$ follows the correct distribution $p[\sigma]$; this process is called *thermalization*. When the thermalization has been achieved, one can start to measure different observables numerically. Between each configuration that is used for measurements one has to apply several updates, because subsequent configurations of the Markov chain are correlated. A quantitative manner to

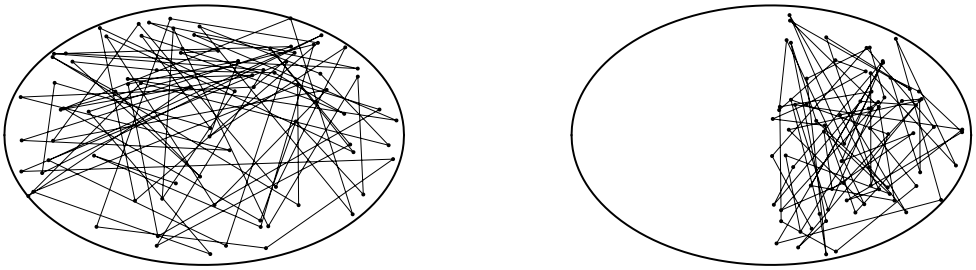

Figure 3.1: In the left-hand graph we sketch an example of an ergodic chain. It reaches the entire sample space. The right-hand graph represents a non-ergodic chain, since it is restricted to only a subset of the sample space.

determine the correlation level of the configurations of our chain and the number of updates to thermalize the system consists of computing the *autocorrelation time* τ. Generally, one seeks an algorithm that has a certain value of τ for the smallest computing (CPU) time possible.

To properly define the autocorrelation time let us consider a set of measurements $\{x_1, x_2, \cdots, x_N\}$ of an observable X. The correlation function at Markov time t is given by

$$C_X(t) = \langle x_i x_{i+t} \rangle - \langle x_i \rangle \langle x_{i+t} \rangle = \frac{1}{N-t} \sum_{i=0}^{N-t-1} x_{i+t}(x_i - \overline{x}_{N-t-1}), \tag{3.11}$$

where

$$\overline{x}_{N-t-1} = \frac{1}{N-t} \sum_{i=0}^{N-t-1} x_i, \quad t = 0, \cdots, N-1. \tag{3.12}$$

For large t, the following decay of the correlation function is generic

$$C_X(t) \propto e^{-t/\tau_{\text{exp}}}, \tag{3.13}$$

where we refer to τ_{exp} as the *exponential autocorrelation time*. It can be obtained by measuring the correlation function of an observable, *e.g.* the energy, and fitting eq. (3.13). In general, τ_{exp} depends on the observable. Thus, to avoid any ambiguity, one considers $\tau_{\text{exp}} = \sup(\{\tau_{\text{exp}}^{\mathcal{O}} | \mathcal{O} \text{ an observable of interest}\})$.

One can also show that τ_{exp} gives an estimate of the number of updates that one has to perform to achieve thermalized configurations (configurations in equilibrium). In particular, it is possible to prove that (see Refs. [48,49]) if P^t is the probability distribution at a time t in the Markov process, π is the equilibrium distribution (the one that is obtained in the $t \to \infty$ limit) and $f(x)$ is a function defined on the sample space Ω with the norm

$$||f(x)|| = \sqrt{\int_\Omega |f(x)|^2 \pi(x) dx}, \tag{3.14}$$

for large t one has

$$\sup\left\{ \left| \int_\Omega f(x) P^t(x) dx - \int_\Omega f(x)\pi(x)dx \right|, \quad ||f(x)|| \leq 1 \right\} \leq \exp(-t/\tau_{\text{exp}}). \tag{3.15}$$

Therefore, τ_{exp} is interpreted as the relaxation time of the system, since for $t \gg \tau_{\text{exp}}$ the chain can be considered to be in equilibrium.

There is another type of autocorrelation time, which is known as the *integrated autocorrelation time*, τ_{int}. For $\tau_{\text{int}} > 1/2$ it is given by

$$\tau_{\text{int}} = \frac{1}{2} + \sum_{t=1}^{N} \frac{C_X(t)}{C_X(0)}. \tag{3.16}$$

For large N the standard error of $\langle X \rangle$ is related to τ_{int} through (see Ref. [49])

$$S_\sigma = \sqrt{\frac{\text{Var(X)}}{N}} = \sqrt{\frac{\langle (X - \langle X \rangle)^2 \rangle}{N}} \approx \sqrt{\frac{2\tau_{\text{int}}}{N} C_X(0)}. \tag{3.17}$$

The statistical error is proportional to the square root of the variance. In this manner, τ_{int} provides a way of finding an error that takes into account correlations between measurements. However, this is not the usual procedure in practice. Instead one uses different methods to compute the error, like the one that we will discuss in the next section. Still, τ_{int} has a useful interpretation: it tells us that we are using an effective sample of $N/2\tau_{\text{int}}$ decorrelated measurements. When $\tau_{\text{int}} \leq 1/2$, the effective sample is N, which indicates a perfect decorrelation. Once again, τ_{int} depends on the observable that we consider, so one has to take $\tau_{\text{int}} = \sup(\{\tau_{\text{int}}^{\mathcal{O}} | \mathcal{O} \text{ an observable of interest}\})$.

In the literature, a distinction between τ_{int} and τ_{exp} is not often made, because for large N and $\tau_{\text{exp}} \gg 1$ both times are proportional. This is seen as follows

$$\tau_{\text{int}} = \frac{1}{2} + \sum_{t=1}^{N} \frac{C_X(t)}{C_X(0)} \approx \frac{1}{2} + A \sum_{t=1}^{\infty} \left(e^{-1/\tau_{\text{exp}}} \right)^t, \tag{3.18}$$

where we used eq. (3.13) and A is a constant. Then

$$\begin{aligned} \tau_{\text{int}} &\approx \frac{1}{2} + A \frac{e^{-1/\tau_{\text{exp}}}}{1 - e^{-1/\tau_{\text{exp}}}} \approx \frac{1}{2} + A \frac{1 - 1/\tau_{\text{exp}}}{1/\tau_{\text{exp}}} \\ &= \frac{1}{2} + A(\tau_{\text{exp}} - 1) \approx A\tau_{\text{exp}}. \end{aligned} \tag{3.19}$$

In systems that exhibit smooth phase transitions, it is known that both τ_{exp} and τ_{int} diverge at the critical point in infinite volume

$$\tau_{\text{exp}} \propto \frac{1}{|T - T_c|^{z_{\text{exp}}\nu}}, \quad \tau_{\text{int}} \propto \frac{1}{|T - T_c|^{z_{\text{int}}\nu}}. \tag{3.20}$$

The exponent z_{exp} is equal to z in eq. (1.37) and ν is the critical exponent of the correlation length. This means that close to the critical point, the number of updates that one has to perform in order to equilibrate the system and to decorrelate the measurements grows indefinitely. This behavior is called *critical slowing down*. Some algorithms, like the cluster algorithms, are very efficient in suppressing this problem because their dynamical critical exponents are small, $z_{\text{int}}, z_{\text{exp}} < 1$, see Refs. [50, 51].

Thus, there are two types of autocorrelation time, each one with a different interpretation. The exponential autocorrelation time tells us how long it takes to equilibrate the system (in Markov time units), while the integrated time is related to the correlation of subsequent configurations in the Markov chain [49]. In practice, the computation of τ is a difficult task. For instance, to determine τ_{exp} one has to fit an exponential decay to the correlation function. However, this decay does not always capture the behavior of the data. In addition, τ_{int} requires a lot of statistics to avoid fluctuations at large t. For these reasons, we we will not address the calculation of τ in this thesis.

3.1.2 Statistical error

To compute the statistical error of an observable obtained with Monte Carlo simulations, one can often not use the standard error. Some observables, like the correlation length, are determined indirectly through fits to the data. In such fits, the standard error is not defined. Furthermore, the computation of S_σ assumes that our measurements are statistically independent. This is not the case in simulations, unless $\tau_{\text{int}} \leq 1/2$. As we mentioned before, one could compute the integrated autocorrelation time to find the error, but its determination is not trivial nor computationally cheap. For this reason, one often uses alternative methods to compute the error of a mean value, considering the possible correlation of data. In particular, we will explain the idea of the *jackknife error*, σ_J, which was used to estimate the uncertainties of the results in this work.

Let us suppose that we have N measurements of a variable x. We describe the calculation of σ_J as a recipe:

- We calculate the average $\langle x \rangle$ of the N measurements.
- We divide the N measurements in M blocks. M should preferably be a number that satisfies $N/M \in \mathbb{N}$.
- For each block $m = 1 \dots M$, we consider the set of the $N - N/M$ measurements without the block m and calculate its average $\langle x \rangle_m$.
- The jackknife error is defined as

$$\sigma_J = \sqrt{\frac{M-1}{M} \sum_{m=1}^{M} \left(\langle x \rangle_m - \langle x \rangle\right)^2}. \tag{3.21}$$

An important remark is that when $M = N$, σ_J coincides with the standard error, since for that case we have

$$\langle x \rangle_m = \frac{1}{N-1} \sum_{m' \neq m}^{N} x_{m'}, \tag{3.22}$$

thus

$$\begin{aligned} \langle x \rangle_m - \langle x \rangle &= \frac{1}{N-1} \sum_{m' \neq m}^{N} x_{m'} - \frac{1}{N} \sum_{m'=1}^{N} x_{m'} \\ &= \frac{1}{N(N-1)} \left(x_1 + \cdots + x_m + \cdots x_N\right) - \frac{1}{N} x_m - \frac{1}{N(N-1)} x_m \\ &= \frac{1}{N-1} \left(\langle x \rangle - x_m\right). \end{aligned} \tag{3.23}$$

Then

$$\sigma_J = \sqrt{\frac{N-1}{N(N-1)^2} \sum_{m=1}^{N} \left(x_m - \langle x \rangle\right)^2} = \sqrt{\frac{1}{N(N-1)} \sum_{m=1}^{N} \left(x_m - \langle x \rangle\right)^2}. \tag{3.24}$$

However, it is not the idea to take $M = N$, but to work with $M \ll N$. In general, σ_J changes for a different number of blocks M and it tends to be somewhat larger than the standard error. Therefore, normally one calculates the right-hand side of eq. (3.21) for several M and chooses the error as the largest value of the σ_J that one obtains.

Further information about Markov chains and its statistical analysis can be found in Refs. [48, 49, 52–54].

3.2 Monte Carlo algorithms

In this section we will explain the implementation of four different algorithms to simulate the XY model. Each one can also be applied to other systems. The codes were self-written with C++. The implementations are available in a GitHub repository [55].

3.2.1 Metropolis algorithm

The Metropolis algorithm was the first importance sampling Monte Carlo algorithm used to simulate statistical mechanics systems [56]. It is also one of the easiest algorithms to implement and has a wide variety of applications. We will explain its implementation for the XY model as a recipe.

1. Create an initial configuration $[\sigma_0]$. This can be done, for instance, by assigning random directions to the spins on the lattice in the range $(-\pi, \pi]$ (*hot start*) or by aligning all the spins in one direction (*cold start*).
2. Pick a site i with spin $\vec{S}_i$ and propose the change $\vec{S}_i \to \vec{S}_i'$, where the direction of $\vec{S}_i'$ is randomly chosen in the interval $(-\pi + \epsilon, \pi - \epsilon]$. One has the freedom to fix ϵ. In this thesis we select $\epsilon = 0$, *i.e.* we consider the full angular range.
3. Accept or reject the update based on the transition probability

$$T(\sigma'|\sigma_0) = \min\left(1, \frac{\exp(-\beta H[\sigma'])}{\exp(-\beta H[\sigma_0])}\right), \tag{3.25}$$

   where $[\sigma_0]$ is the initial configuration and usually $[\sigma']$ only differs at one site i. The transition probability can be implemented as follows: if $\Delta H = H[\sigma'] - H[\sigma_0] > 0$ we generate a random number $r \in (0, 1)$. If $r < \exp(-\beta \Delta H)$, we accept the change. Otherwise, the configuration stays the same. If $\Delta H \leq 0$ we always accept the change.
4. Repeat steps 2 and 3 updating a variety of lattice sites. This can be done randomly or in a lexicographic order. After revising L^d sites, with d dimension of the system and L its linear size, we say that we have performed a *sweep*.

We can verify that the transition probability (3.25) satisfies detailed balance,

$$\begin{aligned} T(\sigma'|\sigma_0)\exp(-\beta H[\sigma_0]) &= \min\left(1, \frac{\exp(-\beta H[\sigma'])}{\exp(-\beta H[\sigma_0])}\right)\exp(-\beta H[\sigma_0]) \\ &= \min\big(\exp(-\beta H[\sigma_0]), \exp\big(-\beta H[\sigma']\big)\big) \\ &= \min\left(1, \frac{\exp(-\beta H[\sigma_0])}{\exp(-\beta H[\sigma'])}\right)\exp\big(-\beta H[\sigma']\big) \\ &= T(\sigma_0|\sigma')\exp\big(-\beta H[\sigma']\big). \end{aligned} \tag{3.26}$$

We used the positivity of all the factors involved to manipulate the minimum.

An application of this algorithm, together with a review of its properties, in the context of quantum mechanics is given in Ref. [57]. The local updates make this algorithm inefficient close to a critical point. Its z_{int} and z_{exp} exponents are approximately 2, see for instance Refs. [58, 59]. This means that the number of thermalization sweeps and updates between measurements has to be very large close to criticality, which increases the CPU time. Still, for simulations out of equilibrium it is particularly useful, as we will explain later in this chapter.

3.2.2 Cluster algorithm

The basic idea of this algorithm is to create *bonds* between neighboring sites with a certain probability criterion. After the bonds have been created throughout the lattice, one identifies the *clusters*. That is, one identifies the sets of sites that are connected through the bonds. Then, to generate a new configuration one collectively reflects the spins of each cluster with respect to a line, with probability one half, see Figure 3.2. In the literature one distinguishes two types of cluster algorithms: the *Swendsen-Wang* or *multi-cluster* algorithm [60], where one identifies all the clusters on the lattice and considers flipping them all, and the *Wolff* or *single-cluster* algorithm [61], where one flips only one cluster for each update with probability one. Both of them generate ergodic Markov chains and satisfy detailed balance, as shown in Refs. [60, 61]. Their implementation is quite similar.

In the following steps we describe the implementation of the multi-cluster algorithm, which we will just refer to as "the cluster algorithm":

1. Begin with a hot or cold start, or any other start.
2. Define a direction with a random vector $\vec{r} \in \mathbb{S}^1$. For two nearest-neighboring spins $\vec{S}_i$ and $\vec{S}_j$, we create a bond with probability
$$p = 1 - \exp\left[-2\beta(\vec{r}\cdot\vec{S}_i)(\vec{r}\cdot\vec{S}_j)\right]. \tag{3.27}$$
We do this step for every pair of nearest neighbors.
3. Once the bonds are created, we identify the clusters. This is technically the most difficult step. When inefficiently done, it can consume a lot of CPU time. There exists, however, an efficient way to do it, which is known as the *Hoshen-Kopelman* algorithm [62]. The advantage of this method is that it can identify the clusters in a computing time only linear in the volume of the system. This algorithm is implemented in our codes for two- and three-dimensional lattices with periodic boundaries.
4. Attempt to reflect the spins of the clusters with respect to the line orthogonal to $\vec{r}$ with some probability, usually $p = 1/2$. In practice this can be done as follows: choose a cluster $\mathcal{C}$ and consider a random number $R \in (0, 1)$. If $R < 1/2$, we collectively change all the spins of $\mathcal{C}$ according to
$$\vec{S}_i \to \vec{S}_i - 2\vec{r}(\vec{r}\cdot\vec{S}_i), \quad \vec{S}_i \in \mathcal{C}. \tag{3.28}$$
Otherwise, the cluster is kept invariant. One repeats this step for all the clusters.
5. Return to step 2.

Steps 2, 3, 4 and 5 conform a sweep with the cluster algorithm. Every time that one repeats step 2, a new random vector $\vec{r} \in \mathbb{S}^1$ is generated, but it remains fixed until the end of step 4.

The cluster algorithm is the best known option to simulate O(N) models in equilibrium, because it deals very efficiently with the critical slowing down. As we mentioned before, its dynamical critical exponent z tends to be very small compared with the Metropolis algorithm, see *e.g.* Refs. [63,64]. In essence, this is due to the fact that the cluster algorithm performs collective updates, *i.e.* one updates entire clusters, instead of modifying site by site like Metropolis. Therefore, decorrelation and thermalization are usually done in less computing time than with local-update schemes. Furthermore, the Hoshen-Kopelman method makes this algorithm efficient. Nevertheless, for simulations out of equilibrium the cluster algorithm is not a very good option, because it tends to equilibrate the system very quickly. Moreover, this does not coincide with the real process in nature, which is supposed to be local.

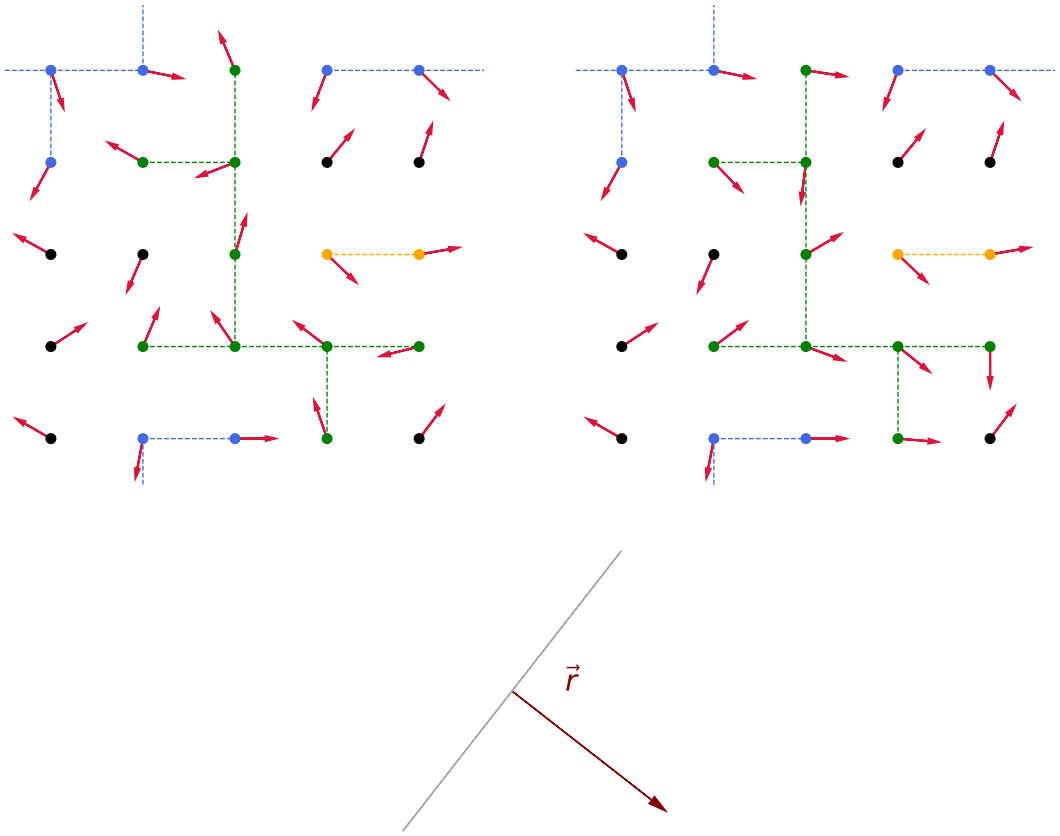

Figure 3.2: In the upper-left panel we show a configuration where some spins have been linked by bonds with a probability given by eq. (3.27). Notice the periodic boundaries, which are manifest in the bonds. The different colors represent the clusters. The black points are clusters of one element. The upper-right panel shows the result after reflecting the green cluster with respect to the orthogonal line to a random vector $\vec{r}$.

3.2.3 Heatbath algorithm

The heatbath algorithm is another local-update scheme, which was first used to simulate pure gauge theories as an improvement compared to Metropolis. In the beginning, it was implemented for a pure SU(2) gauge theory [65] and later for SU(3) [66] and SU(N) [67]. In Ref. [68] the first implementation of this algorithm in classical spin models is shown, before the invention of the cluster algorithm. It is somewhat more efficient than Metropolis but less than the cluster algorithm, see *e.g.* Ref. [69]. To explain the implementation consider the contribution to the Hamiltonian, in units of $J = 1$, at a site x on the lattice

$$H_x = -\vec{S}_x \cdot \sum_{\pm\mu} \vec{S}_{x+\hat{\mu}} = -\vec{S}_x \cdot \vec{\sigma}_x = -S_x \sigma_x \cos\theta = -\sigma_x \cos\theta, \tag{3.29}$$

where $\vec{\sigma}_x$ is the vector sum of all the spin neighbors of $\vec{S}_x$, θ is the angle between $\vec{\sigma}_x$ and $\vec{S}_x$ and $|\vec{S}_x| = S_x$, $|\vec{\sigma}_x| = \sigma_x$. The probability of having this spin orientation, *i.e.* the angle θ at x, is

$$P_x(\theta) = \frac{\exp(-\beta H_x(\theta))}{\int_{-\pi}^{\pi} \exp(-\beta H_x(\theta'))d\theta'}. \tag{3.30}$$

The idea of the heatbath algorithm is to update the angle $\theta \to \varphi$ based on this probability distribution. To do so one could generate a random number $r \in (0, 1)$ and solve the equation

$$r = \int_{-\pi}^{\varphi} P_x(\theta')d\theta' \tag{3.31}$$

for φ. Then the spin at the site x is changed, $\theta \to \varphi$. An update of every site or the same number of random sites conforms a sweep.

Solving eq. (3.31) cannot be done analytically for this particular model. Therefore one has to numerically compute φ. For fixed β (simulation in equilibrium) one can calculate φ for numerous values of r and make a lookup table. However, in simulations out of equilibrium β changes in each sweep and numerically integrating eq. (3.31) for each spin update consumes a lot of CPU time. To deal with this problem we will use the *Hattori-Nakajima* algorithm [70], which enables us to obtain angles distributed according to eq. (3.30).

The Hattori-Nakajima algorithm adopts the *rejection method* [70]. The idea is to find a normalized distribution $\tilde{P}_x(\theta)$ that approximates eq. (3.30), *i.e.* a function that interpolates the real distribution $P_x(\theta)$ between $\beta H_x = 0$ and $\beta H_x = \infty$. With $\tilde{P}_x$ one defines a monotonically increasing function $h(z) : (0,1] \to (-\pi, \pi]$ with the property

$$\tilde{P}_x(h(z))\, h'(z) = 1, \quad \forall z \in (0,1], \tag{3.32}$$

where h' is the derivative of h. One also defines

$$g(z) = R(\beta H_x) \frac{P_x(h(z))}{\tilde{P}_x(h(z))}, \quad z \in (0,1],$$

$$R(\beta H_x) = \min\left(\left\{ \frac{\tilde{P}_x(\theta)}{P_x(\theta)} \middle| \theta \in (-\pi, \pi] \right\} \right). \tag{3.33}$$

Appendix A of Ref. [70] proves the following. Let $\{\omega\}$ and $\{\omega'\}$ be two independent sequences of uniform random numbers in the interval $(0,1]$. Define an ordered subsequence of $\{\omega\}$, name it $\{\tilde{\omega}\}$, by selecting those numbers that satisfy

$$\omega' \leq g(\omega). \tag{3.34}$$

Then the sequence

$$h(\tilde{\omega}_1),\, h(\tilde{\omega}_2),\, h(\tilde{\omega}_3), \cdots \tag{3.35}$$

follows the distribution given by eq. (3.30). The same reference proposes a $\tilde{P}_x(\theta)$ and $h(z)$ such that one can generate random numbers distributed according to P_x by following these steps:

1. Define $a = \beta H_x$ and

$$\alpha(a) = \min\left\{ \sqrt{a(2-\epsilon)}, \max\{\sqrt{\epsilon a}, \delta(a)\} \right\},$$
$$\gamma(a) = \max\left\{ \frac{\alpha(a)^2}{a}, \frac{\cosh(\pi\alpha(a)) - 1}{\exp(2a) - 1} \right\} - 1, \tag{3.36}$$

where

$$\delta(a) = 0.35 \max\{0, a - a^*\} + 1.03\sqrt{\max\{0, a - a^*\}}$$
$$\epsilon = 0.001, \quad a^* = 0.798953686083986. \tag{3.37}$$

Define also

$$h(z) = \frac{2}{\alpha(a)} \tanh^{-1}\left\{ \sqrt{\frac{1+\gamma(a)}{1-\gamma(a)}} \tan\left[(2z-1) \tan^{-1}\left(\sqrt{\frac{1-\gamma(a)}{1+\gamma(a)}} \tanh\frac{\pi\alpha(a)}{2} \right) \right] \right\}$$
$$g(z) = \exp\left[-aG(h(z)) \right], \tag{3.38}$$

where

$$G(\theta) = 1 - \cos\theta - \frac{1}{a}\ln\left[1 + \frac{1}{1+\gamma(a)}\Big(\cosh(\alpha(a)\theta) - 1\Big)\right]. \tag{3.39}$$

2. Generate two random numbers, ω and ω', with uniform distribution in the interval $(0, 1]$.
3. If $\omega' \leq g(\omega)$ we can safely say that $h(\omega)$ is distributed according to (3.30). Otherwise, we return to step 2.

Therefore, the implementation of the heatbath algorithm reduces to applying these three steps to every spin on the lattice, where $h(\omega)$ would be identified with the new angle between the spin at the site x and $\vec{\sigma}_x$. One has to derive the spin angle with respect to the horizontal axis by properly transforming θ.

3.2.4 Worm algorithm

The last algorithm that we will discuss is the worm algorithm, which was introduced by Prokof'ev and Svistunov in 2001 [71]. The idea is to work in a dual space to the spin space and to sample configurations there. Before commenting more on the implementation, we have to rewrite the partition function in terms of the variables of this dual space. Let us recall that the Hamiltonian is given by

$$H = -\sum_{\langle ij\rangle} \vec{S}_i \cdot \vec{S}_j \tag{3.40}$$

in units of $J = k_B = 1$. Thus, the partition function is

$$\begin{aligned} Z &= \prod_{k=1}^{N} \int_0^{2\pi} \frac{d\theta_k}{2\pi} \exp\left[\beta \sum_{\langle ij\rangle} \cos(\theta_i - \theta_j)\right] \\ &= \prod_{k=1}^{N} \int_0^{2\pi} \frac{d\theta_k}{2\pi} \prod_{\langle ij\rangle} \exp\left[\beta\cos(\theta_i - \theta_j)\right]. \end{aligned} \tag{3.41}$$

If we use the following identity

$$\sum_{\nu=-\infty}^{\infty} I_\nu(\beta)\exp(i\nu\theta) = \exp(\beta\cos\theta), \tag{3.42}$$

where $I_\nu(\beta)$ is the modified Bessel function of the first kind of order ν, we can rewrite Z as

$$Z = \prod_{k=1}^{N} \int_0^{2\pi} \frac{d\theta_k}{2\pi} \prod_{\langle ij\rangle} \left(\sum_{J_{ij}=-\infty}^{\infty} I_{J_{ij}}(\beta)\exp\left[iJ_{ij}(\theta_i - \theta_j)\right] \right). \tag{3.43}$$

The next step is to integrate over the angles. To do so we will consider, for simplicity, a one-dimensional lattice with N sites and periodic boundary, but the final result will be valid for a general dimension d. Then

$$\begin{aligned} Z = &\prod_{k=1}^{N} \int_0^{2\pi} \frac{d\theta_k}{2\pi} \sum_{J_{12}=-\infty}^{\infty} \sum_{J_{23}=-\infty}^{\infty} \cdots \sum_{J_{N1}=-\infty}^{\infty} I_{J_{12}}(\beta)\exp\left[iJ_{12}(\theta_1 - \theta_2)\right] I_{J_{23}}(\beta) \\ &\times \exp\left[iJ_{23}(\theta_2 - \theta_3)\right] \times \cdots \times I_{J_{N1}}(\beta)\exp\left[iJ_{N1}(\theta_N - \theta_1)\right] \\ = &\sum_{\{J_{ij}\}} I_{J_{12}}(\beta) I_{J_{23}}(\beta) \cdots I_{J_{N1}}(\beta) \int_0^{2\pi} \cdots \int_0^{2\pi} \frac{d\theta_1 d\theta_2 \ldots d\theta_N}{(2\pi)^N} \exp\left[i\theta_1\left(J_{12} - J_{N1}\right)\right] \\ &\times \exp\left[i\theta_2\left(J_{23} - J_{12}\right)\right] \times \cdots \times \exp\left[i\theta_N\left(J_{N1} - J_{(N-1)N}\right)\right], \end{aligned} \tag{3.44}$$

where we define

$$\sum_{\{J_{ij}\}} \equiv \sum_{J_{12}=-\infty}^{\infty} \sum_{J_{23}=-\infty}^{\infty} \cdots \sum_{J_{N1}=-\infty}^{\infty} . \tag{3.45}$$

We will interpret the variable J_{ij} as the *flux* that passes from the site i to j. Thus, we can think of J_{ij} as the number of lines that enter or emanate from the site i in the direction of j. For instance, we can add up $+1$ to the flux J_{ij} if a line coming from j enters the site i, while we add -1 if a line exits from i towards j. With this interpretation, we can also write $J_{ji} \equiv -J_{ji}$, *i.e.* the flux from i to j is minus the flux from j to i. Then

$$\begin{aligned} Z &= \sum_{\{J_{ij}\}} I_{J_{12}}(\beta) I_{J_{23}}(\beta) \cdots I_{J_{N1}}(\beta) \int_0^{2\pi} \cdots \int_0^{2\pi} \frac{d\theta_1 d\theta_2 \ldots d\theta_N}{(2\pi)^N} \exp\left[i\theta_1 \left(J_{12} + J_{1N}\right)\right] \\ &\times \exp\left[i\theta_2 \left(J_{23} + J_{21}\right)\right] \times \cdots \times \exp\left[-i\theta_N \left(J_{N(N-1)} + J_{N1}\right)\right] \\ &= \sum_{\{J_{ij}\}} I_{J_{12}}(\beta) I_{J_{23}}(\beta) \cdots I_{J_{N1}}(\beta) \int_0^{2\pi} \cdots \int_0^{2\pi} \frac{d\theta_1 d\theta_2 \ldots d\theta_N}{(2\pi)^N} \exp\left[i\theta_1 \boldsymbol{\nabla} \cdot \mathbf{J}_1\right] \times \\ &\exp\left[i\theta_2 \boldsymbol{\nabla} \cdot \mathbf{J}_2\right] \times \cdots \times \exp\left[i\theta_N \boldsymbol{\nabla} \cdot \mathbf{J}_N\right], \end{aligned} \tag{3.46}$$

where $\boldsymbol{\nabla} \cdot \mathbf{J}_i \equiv \sum_j J_{ij}$ is the divergence at the site i. Integrating over the angles we see that only when $\boldsymbol{\nabla} \cdot \mathbf{J}_i = 0$, $\forall i = 1, \ldots, N$ (Gauss's law without sources) the configuration contributes to the partition function. Therefore

$$\begin{aligned} Z &= \sum_{\{J_{\rm CP}\}} I_{J_{12}}(\beta) I_{J_{23}}(\beta) \cdots I_{J_{N1}}(\beta) \\ &= \sum_{\{J_{\rm CP}\}} \prod_{\langle ij \rangle} I_{J_{ij}}(\beta), \end{aligned} \tag{3.47}$$

where $\{J_{\rm CP}\}$ stands for *closed path configuration*, which means that the configuration satisfies $\boldsymbol{\nabla} \cdot \mathbf{J}_i = 0$ for $i = 1, \ldots, N$. The expression for Z shown in eq. (3.47) is valid in general space dimension d. The extension is straightforward. It is usual to refer to eq. (3.47) as the *flow representation* of Z.

With the interpretation that we gave to the variables J_{ij}, we can depict the configurations that contribute to the partition function as sets of sites x, where at each x the number of lines that exits is the same as the number of lines that enters (flux at x equal to zero), see Figure 3.3 (a).

The worm algorithm samples a larger space than the one corresponding to Z. This space is defined by those configurations that contribute to the correlation function between two sites I and M

$$\begin{aligned} G = Z\langle \vec{S}_I \cdot \vec{S}_M \rangle &= \int_0^{2\pi} \int_0^{2\pi} \frac{d\theta_I d\theta_M}{(2\pi)^2} \prod_{k \neq I,M}^{N} \int_0^{2\pi} \frac{d\theta_k}{2\pi} \vec{S}_I \cdot \vec{S}_M \prod_{\langle ij \rangle} \exp\left[\beta \cos(\theta_i - \theta_j)\right] \\ &= \int_0^{2\pi} \int_0^{2\pi} \frac{d\theta_I d\theta_M}{(2\pi)^2} \prod_{k \neq I,M}^{N} \int_0^{2\pi} \frac{d\theta_k}{2\pi} \cos(\theta_I - \theta_M) \prod_{\langle ij \rangle} \exp\left[\beta \cos(\theta_i - \theta_j)\right]. \end{aligned} \tag{3.48}$$

By performing similar steps as with the partition function, it can be proved that the correlation function takes the form

$$G = \sum_{\{J_{\rm OP}\}} \prod_{\langle ij \rangle} I_{J_{ij}}(\beta), \tag{3.49}$$

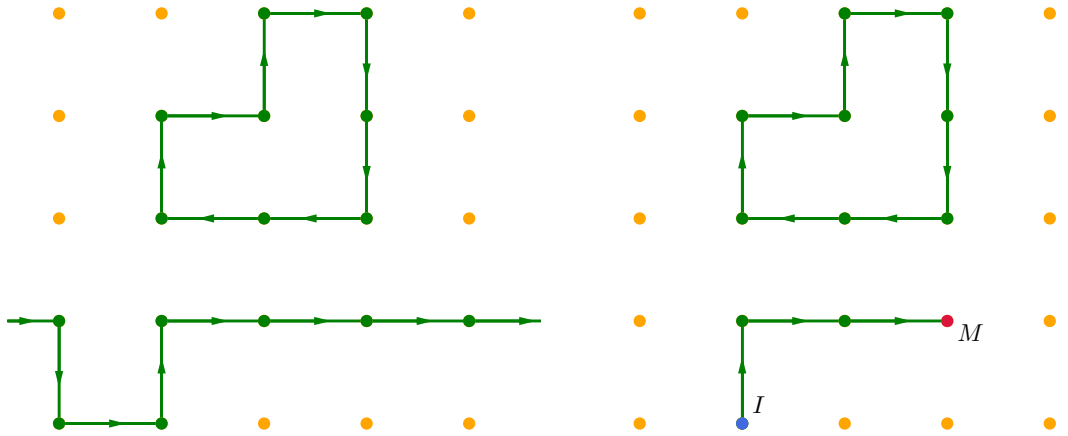

(a) (b)

Figure 3.3: Diagram (a) shows a configuration that contributes to the partition function in the flow representation, notice the periodic boundary. At each site, the number of lines that emanate is equal to the number of lines that enter, *i.e.* the divergence is zero. Diagram (b) depicts a configuration that contributes to the correlation function. We observe that the flux is zero at each site, except at I, where $\boldsymbol{\nabla}\cdot\mathbf{J}_I = -1$ and at M, where $\boldsymbol{\nabla}\cdot\mathbf{J}_M = 1$.

where $\{J_{\mathrm{OP}}\}$ stands for *open path configuration*. This refers to the configurations where $\boldsymbol{\nabla}\cdot\mathbf{J}_i = 0$, $\forall i \neq I, M$ and $\boldsymbol{\nabla}\cdot\mathbf{J}_{M,I} = \pm 1$. A graphical example is shown in Figure 3.3 (b).

The idea of the worm algorithm is to sample the G-space in such a way that when $I = M$ we recover a configuration of the Z-space. This is achieved by following these steps:

1. Select a random site on the lattice and fix there $I = M$.
2. Choose one of the neighbors of M, say N, and propose an update of the flux from J_{MN} to $J'_{MN} = J_{MN} + 1$ (note that this also modifies the flux at N).
3. Accept the update with probability

$$p = \min\left(1, \frac{I_{J'_{MN}}(\beta)}{I_{J_{MN}}(\beta)}\right), \tag{3.50}$$

   where I_J is a Bessel function of the first kind of order J. If the update is accepted, we move from M to N (I does not move); otherwise we repeat the previous step.
4. Repeat steps 2 and 3 until $I = M$. When this happens, we go back to step 1.

After performing these steps several times one obtains configurations in the flow representation that are distributed according to H. The fact that one leaps from configurations in the G-space to configurations in the Z-space makes this algorithm very efficient. In Ref. [71] the dynamical critical exponent is found to be $z = 0.2$ for the 3d XY model and $z = 0.16$ for the 2d XY model.

When the system is thermalized, we can measure observables. This is, however, usually hard with the worm algorithm, because the degrees of freedom are not spins anymore, but flux variables. Therefore, one has to find an equivalent way to measure the observables in

terms of J_{ij}. For instance, the expectation value of the energy is given by

$$\langle E\rangle = -\frac{1}{Z}\frac{\partial Z}{\partial \beta}. \tag{3.51}$$

To find an expression for $\langle E\rangle$ in terms of J_{ij} we consider the one-dimensional case. Once again, the final result will be valid in any dimension and the proof is just a generalization. Then

$$Z = \sum_{\{J_{\rm CP}\}} I_{J_{12}(\beta)} I_{J_{23}(\beta)} \cdots I_{J_{N1}(\beta)}. \tag{3.52}$$

By computing the derivative with respect to β we obtain

$$\begin{aligned}\frac{\partial Z}{\partial \beta} = \sum_{\{J_{\rm CP}\}} \Big(& I'_{J_{12}}(\beta) I_{J_{23}}(\beta)\cdots I_{J_{N1}}(\beta) + I_{J_{12}}(\beta) I'_{J_{23}}(\beta)\cdots I_{J_{N1}}(\beta) + \cdots \\ & + I_{J_{12}}(\beta) I_{J_{23}}(\beta)\cdots I'_{J_{N1}}(\beta)\Big) \\ = \sum_{\{J_{\rm CP}\}} & \left(\frac{I'_{J_{12}}(\beta)}{I_{J_{12}}(\beta)} + \frac{I'_{J_{23}}(\beta)}{I_{J_{23}}(\beta)} + \cdots + \frac{I'_{J_{N1}}(\beta)}{I_{J_{N1}}(\beta)}\right) I_{J_{12}}(\beta) I_{J_{23}}(\beta)\cdots I_{J_{N1}}(\beta).\end{aligned} \tag{3.53}$$

Therefore

$$\langle E\rangle = -\left\langle \sum_{\langle ij\rangle} \frac{I'_{J_{ij}}(\beta)}{I_{J_{ij}}(\beta)} \right\rangle. \tag{3.54}$$

This equation provides a way to measure the energy with the worm algorithm. One is often interested in determining the specific heat

$$C_V = -\frac{1}{V}\beta^2 \frac{\partial \langle E\rangle}{\partial \beta} = \beta^2 \frac{\langle E^2\rangle - \langle E\rangle^2}{V} \tag{3.55}$$

as well. Then, an expression for $\langle E^2\rangle$ in terms of the flux variables is also needed. To find it we calculate

$$\langle E^2\rangle = \frac{1}{Z}\frac{\partial^2 Z}{\partial \beta^2}. \tag{3.56}$$

By using eq. (3.52) we have

$$\begin{aligned}\langle E^2\rangle = \Bigg\langle & \frac{I''_{J_{12}}(\beta)}{I_{J_{12}}(\beta)} + \cdots + \frac{I''_{J_{N1}}(\beta)}{I_{J_{N1}}(\beta)} - \left(\frac{I'_{J_{12}}(\beta)}{I_{J_{12}}(\beta)}\right)^2 - \cdots - \left(\frac{I'_{J_{N1}}(\beta)}{I_{J_{N1}}(\beta)}\right)^2 \\ & + \left(\frac{I'_{J_{12}}(\beta)}{I_{J_{12}}(\beta)} + \cdots + \frac{I'_{J_{N1}}(\beta)}{I_{J_{N1}}(\beta)}\right)^2 \Bigg\rangle.\end{aligned} \tag{3.57}$$

Therefore, for general d

$$\langle E^2\rangle = \left\langle \sum_{\langle ij\rangle} \frac{I''_{J_{ij}}(\beta)}{I_{J_{ij}}(\beta)} \right\rangle - \left\langle \sum_{\langle ij\rangle} \left(\frac{I'_{J_{ij}}(\beta)}{I_{J_{ij}}(\beta)}\right)^2 \right\rangle + \left\langle \left(\sum_{\langle ij\rangle} \frac{I'_{J_{ij}}(\beta)}{I_{J_{ij}}(\beta)} \right)^2 \right\rangle. \tag{3.58}$$

Unfortunately, other observables, like the density of vortices, are not easily computable in this formulation. We did not find a way to transform the flux variables back to spins either. For these reasons, we do not use the worm algorithm to study the dynamics of the topological defects of the XY model in this thesis. Still, it is useful to compare some of the results with the other algorithms as a cross-check and their efficiency.

This algorithm is also applicable to quantum field theories, see *e.g.* Refs. [72, 73], but it suffers from the same problem: it is not possible to find an equivalent way to measure expectation values for arbitrary observables and there is no general procedure to find a dual space to simulate.

Chapter 4

Simulations of the 2d XY model

In this chapter we present simulation results of the 2d XY model in equilibrium and out of equilibrium. In the simulations in equilibrium we compare the four algorithms to show that we always obtain the same results, which guarantees that our implementations are correct.

4.1 Simulations in equilibrium

We show results of the energy density, magnetization density, specific heat, magnetic susceptibility and vortex density measured with the Metropolis, cluster and heatbath algorithm. We work with lattices of volume L^2, with $L = 8, 16, 24, 32$ and 64. We thermalize the system with 10^3 sweeps starting with a hot start (see Section 3.2 for a definition of sweep for each algorithm) and perform 10^4 measurements, separated by 50 decorrelation sweeps in all the cases.

With the worm algorithm, we only determine the energy density and the specific heat. For this algorithm we discarded the first 10^3 configurations of the Z-space to achieve the thermalization. We do not make decorrelation updates either, because at each step the system jumps from the Z-space to the G-space. We use 10^5 configurations to perform measurements for $L = 8, 16, 24$ and 32, while for $L = 64$ we use 10^6 configurations.

In Figure 4.1, we present the energy density, magnetization density, specific heat and magnetic susceptibility for a lattice with $L = 24$. In general we see a perfect agreement between the algorithms. The energy and magnetization density are very stable observables, thus we do not see any discrepancy. However, for C_V and χ_M we observe that close to the critical temperature of the BKT transition [74, 75],

$$T_c = 0.89290(5), \quad \beta_c = 1.11994(6), \tag{4.1}$$

these observables do not perfectly agree for the different algorithms. This is an effect of the high autocorrelations in the neighborhood of the critical point. To achieve a better agreement we would need to increase the number of decorrelation sweeps. In Figure 4.2 we present the same results but for a larger lattice, $L = 32$.

In Figure 4.3, we show the density of vortices, ρ_V, and the density of anti-vortices, ρ_{AV}, measured with the cluster, Metropolis and heatbath algorithms for $L = 64$. To determine the vorticity we used eq. (2.32) for each plaquette. This observable does not show strong autocorrelation effects, as we can see in Figure 4.3 (d), where all the algorithms coincide. We observe that ρ_V is numerically equal to $-\rho_{AV}$. This is consistent with the fact that with periodic boundary conditions the number of vortices must be equal to the number

of anti-vortices, as pointed out in Chapter 2. For this reason, in the continuation we will only study the behavior of ρ_V.

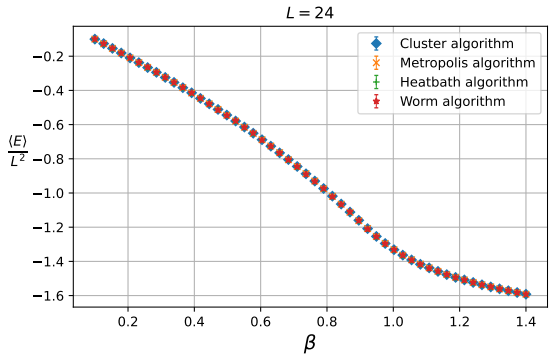

(a) Energy density

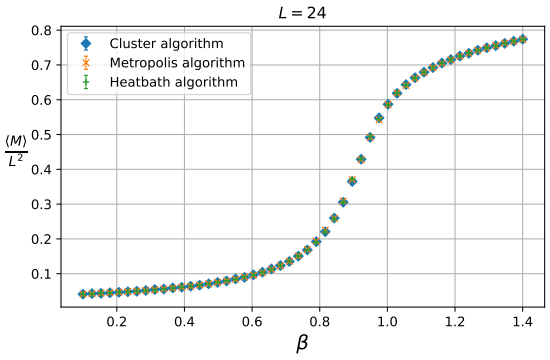

(b) Magnetization density

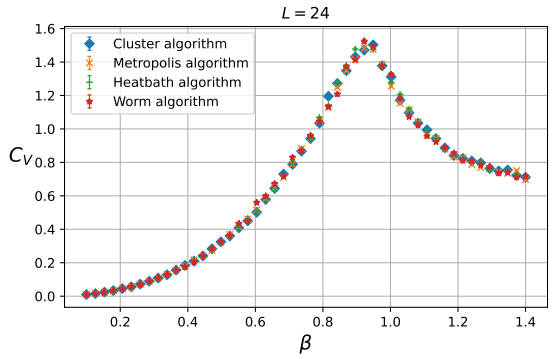

(c) Specific heat

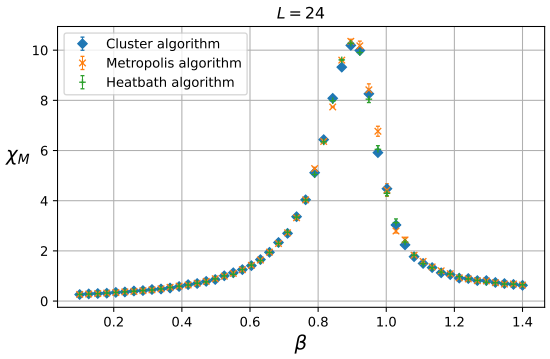

(d) Magnetic susceptibility

Figure 4.1: Observables measured with different algorithms for a lattice of size 24×24. With the worm algorithm we only compute $\langle E \rangle$ and C_V. For the energy and the magnetization density we see perfect agreement between all the algorithms. For C_V and χ_M we observe small discrepancies close to the critical point of the BKT transition, $\beta_c = 1.11994(6)$. The latter shows that the specific heat and the magnetic susceptibility are more sensitive to autocorrelation effects and that we would need more decorrelation sweeps to obtain exactly the same results.

Figure 4.4 shows results of χ_M measured with the cluster, Metropolis and heatbath algorithm for several lattice sizes. We also present results of C_V for several lattice sizes with the worm algorithm. We observe that the peak of C_V does not have a strong dependence on L. On the other hand, the increasing peak in χ_M is more noticeable and it is attributed to the phase transition. For large volumes, the position of the peak indicates the critical temperature. In Figure 4.4 (a) we see that the peak's position shifts to $\beta \simeq 1.12$ as the volume increases. Ref. [76] provides the scaling of this position in terms of L. By naming T^* to the temperature that corresponds to the maximum of χ_M, Ref. [76] provides

$$T^* \simeq T_c + \frac{A}{(\ln L)^2}, \tag{4.2}$$

where T_c is the critical temperature and A is a constant. Our data shows a very good agreement with this scaling, as we exhibit in Figure 4.5. With eq. (4.2) one can attempt to determine T_c. Our fit yields

$$T_c = 0.915(2). \tag{4.3}$$

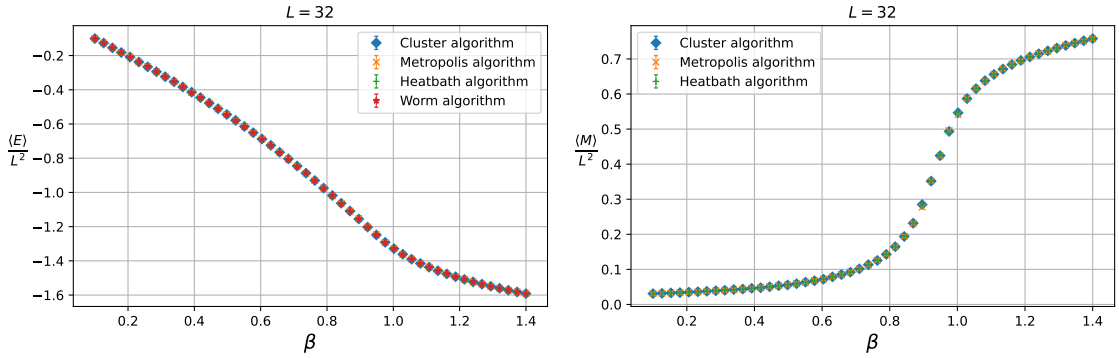

(a) Energy density

(b) Magnetization density

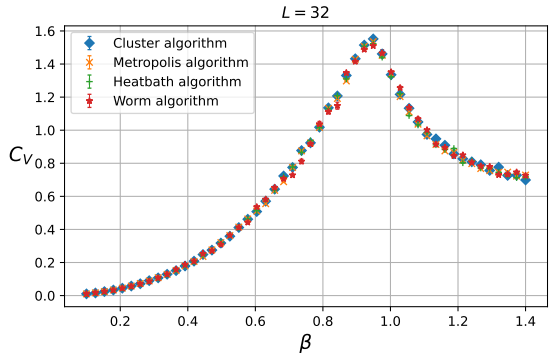

(c) Specific heat

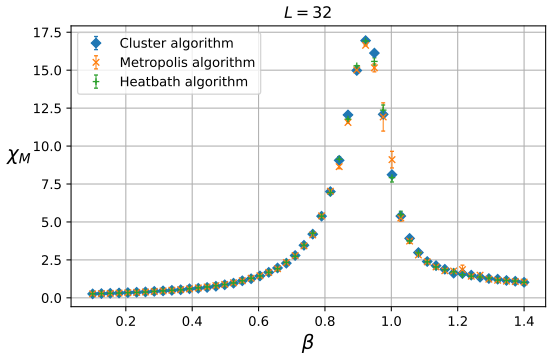

(d) Magnetic susceptibility

Figure 4.2: Observables measured with different algorithms for a lattice of size 32×32. We observe that the peak of χ_M increases with the volume (see Figure 4.1 for reference). This is due to the phase transition.

This value is slightly different than the one reported with high precision in Refs. [74, 75], see eq. (4.1). To achieve a better compatibility we would need to consider larger volumes and higher statistics.

At last, in Figure 4.4 (d) we see that the results of $L = 64$ are plagued with large error bars, which were computed with the jackknife method. This is once again due to the autocorrelation effects that the Metropolis algorithm is more sensitive to have. Such effects become stronger with increasing volume. To achieve better results we would need more decorrelation steps for this particular algorithm. Still, this is consistent with what we mentioned before: Metropolis is highly inefficient to deal with autocorrelation, close to criticality.

4.2 Simulations out of equilibrium

Now we describe a way to simulate a cooling process. We only study the dynamics of the density of vortices, ρ_V. This will be the main focus of the next chapter in the 3d model. We present the main ideas here for the two-dimensional XY model, which has been analyzed in this context before, in particular in Ref. [77]. This allows us to compare results.

First, we need to define a way to lower the temperature of the system with *time*. We will interpret a sweep as a unit of time. Notice that this unit depends on the algorithm that we choose. Then, in order to compare with the results of Ref. [77] and also inspired

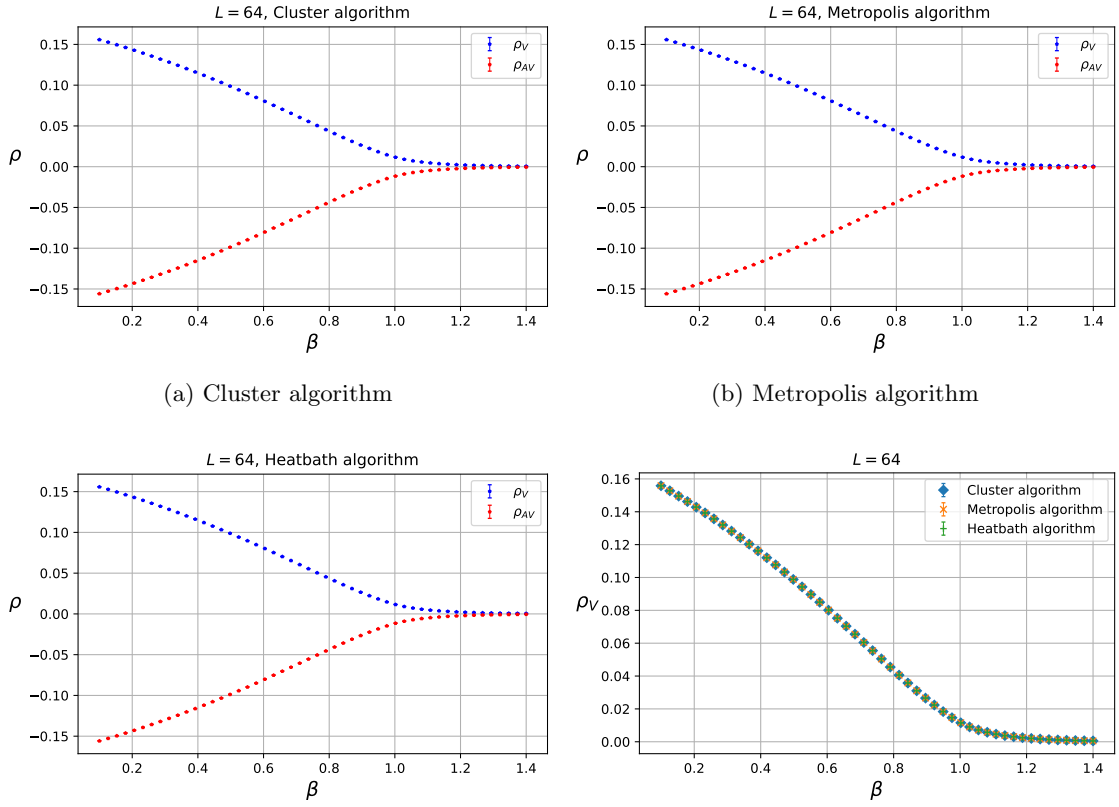

(a) Cluster algorithm

(b) Metropolis algorithm

(c) Heatbath algorithm

(d) Comparison between algorithms

Figure 4.3: Comparison of the density of vortices and anti-vortices for a lattice of size 64×64. The results were obtained with the cluster, Metropolis and heatbath algorithm. We did not find any way to compute the vorticity of a plaquette with the worm algorithm. We observe a perfect agreement between the algorithms. In addition, we see that ρ_V is exactly equal to $-\rho_{AV}$, as it should be for periodic boundary conditions. The vorticity was measured by using eq. (2.32).

by eq. (1.38) of the Zurek mechanism, we adopt the following linear quenching scheme

$$T(t) = T_c \left(1 - \frac{t - \tau_Q}{\tau_Q}\right), \quad t \in [0, 2\tau_Q]\,. \tag{4.4}$$

We start at $T = 2T_c$ and we linearly reduce the temperature down to $T = 0$. Notice that our time t only takes integer values. If τ_Q is long, we perform a *slow cooling*. As a consequence, the system is quasi-adiabatic at each instant of time before the phase transition, so the values of our observables are expected to remain the same as in equilibrium. On the other hand, if τ_Q is short, we apply a *fast cooling*. Then, the quenching is out of equilibrium at almost any instant of time.

In any case, it is impossible to maintain the equilibrium for all t, because of the BKT transition, so either way the system will leave equilibrium in a vicinity of T_c.

To simulate a cooling process we first thermalize the system at $2T_c$ ($t = 0$). This can be done with the cluster, heatbath or Metropolis algorithm, but it is preferable to use the cluster algorithm because it is most efficient. We then apply eq. (4.4) to reduce the temperature according to the number of sweeps that we are performing. The result of this procedure will be different for distinct algorithms, because each one thermalizes (equilibrates) the system at a different rate. Here it is not appropriate to perform decorrelation

sweeps, because by doing so we would equilibrate the system at each instant of the cooling, which we want to avoid. To generate a good statistics, we have to repeat this same process many times and measure ρ_V for all t.

In Figure 4.6 we show the evolution of the density of vortices with time for $\tau_Q = 8$ (fast cooling) and $\tau_Q = 512$ (slow cooling). We compare the outcome of the process when using the Metropolis or cluster algorithm. We performed the cooling 10^3 times, starting each time in a different equilibrium configuration. We observe that before the phase transition both algorithms give essentially the same result. This is more noticeable for $\tau_Q = 512$, because the quenching is almost adiabatically. However, in the vicinity of $t = \tau_Q$, which corresponds to $T = T_c$ (see eq. (4.1)), the evolution splits. This is a sign that the system is leaving equilibrium. For $t > \tau_Q$ ($T < T_c$), the density of vortices measured with the cluster algorithm tends to approach to zero faster than with the Metropolis algorithm. This is due to the fact that the cluster algorithm is highly efficient, so it thermalizes the system quickly, which in turn moves ρ_V close to its equilibrium value (for $T < T_c$ the equilibrium value of ρ_V is close to zero). In other words, the cluster algorithm tends to destroy the vortices faster than the Metropolis algorithm during a quenching, with respect to the number of sweeps. Therefore, if one is interested in studying the remaining density of vortices for a temperature lower than T_c, it is better to use the Metropolis algorithm, another local-update scheme or the single-cluster algorithm.

In Ref. [77] the dependence of $\rho_V(T = 0)$ on τ_Q is studied with the Metropolis algorithm. It is observed that it follows a logarithmic decay for very short τ_Q, but at large τ_Q it turns into a power-law. For large L and τ_Q that work reports $\rho_V(T = 0) \propto \tau_Q^{-0.72}$. We attempt to verify this result by using our implementation of the Metropolis algorithm. In the upper plot of Figure 4.7, we show the evolution of the density of vortices for a lattice with $L = 100$ and several values of τ_Q. By using the point that corresponds to the largest t, *i.e.* the density at $T = 0$, we plot $\rho_V(T = 0)$ vs. τ_Q in the lower panel of Figure 4.7. If we perform a power-law fit we obtain $\rho_V \propto \tau_Q^b$, with $b = -0.746(13)$. Thus, our result is compatible, within two sigmas, with the one of Ref. [77].

For the 2d XY model we do not try to verify Zurek's prediction, eq. (1.43), because in two dimensions the transition is not second order, as we explained in Chapter 2. Therefore, the estimate that Zurek gives for the density of topological defects is not supposed to be valid. Still, we observe a power-law behavior for the remnant density of vortices after the cooling and it is worth to consider the exponents. In the next chapter we will study the 3d version of this model, which does have a second order phase transition. We will apply the same method presented here to study the evolution of ρ_V during a cooling process, but with the inclusion of the heatbath algorithm and more lattice sizes.

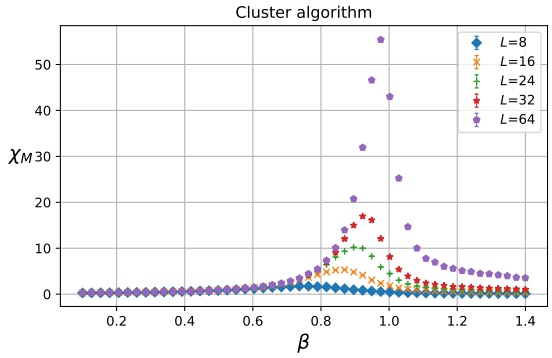

(a) Magnetic susceptibility, cluster algorithm

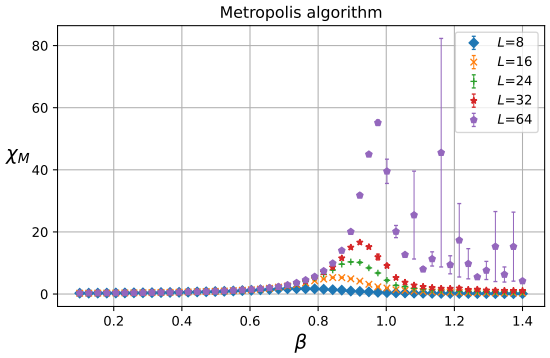

(b) Magnetic susceptibility, Metropolis algorithm

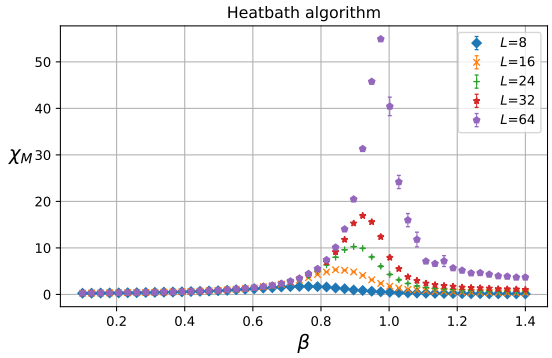

(c) Magnetic susceptibility, heatbath algorithm

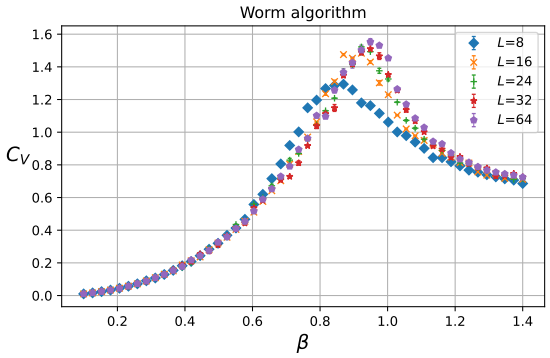

(d) Specific heat, worm algorithm

Figure 4.4: Comparison of the observables for several lattice sizes and different algorithms. For $L = 64$, the magnetic susceptibility measured with the Metropolis algorithm has large error bars and strange values for $\beta > \beta_c$. This indicates a problem with autocorrelated measurements. We observe that as the volume gets larger, the peak in χ_M shifts close to $\beta_c \simeq 1.12$.

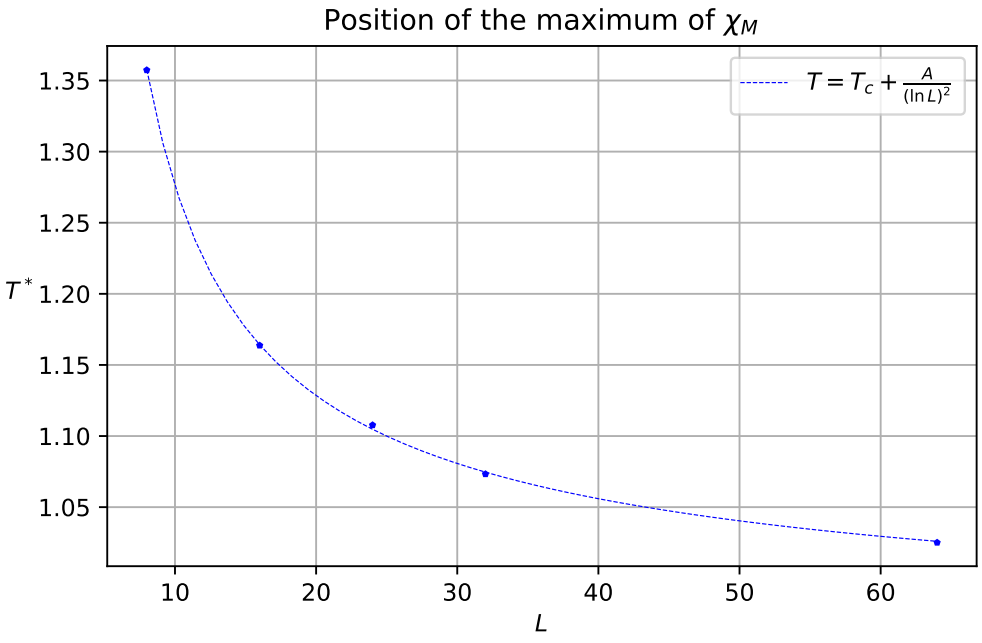

Figure 4.5: Position of the maximum of χ_M for several volumes. We observe a behavior consistent with the one reported in Ref. [76]. The fit constants we obtain are $T_c = 0.915(2)$ and $A = 1.9(1)$

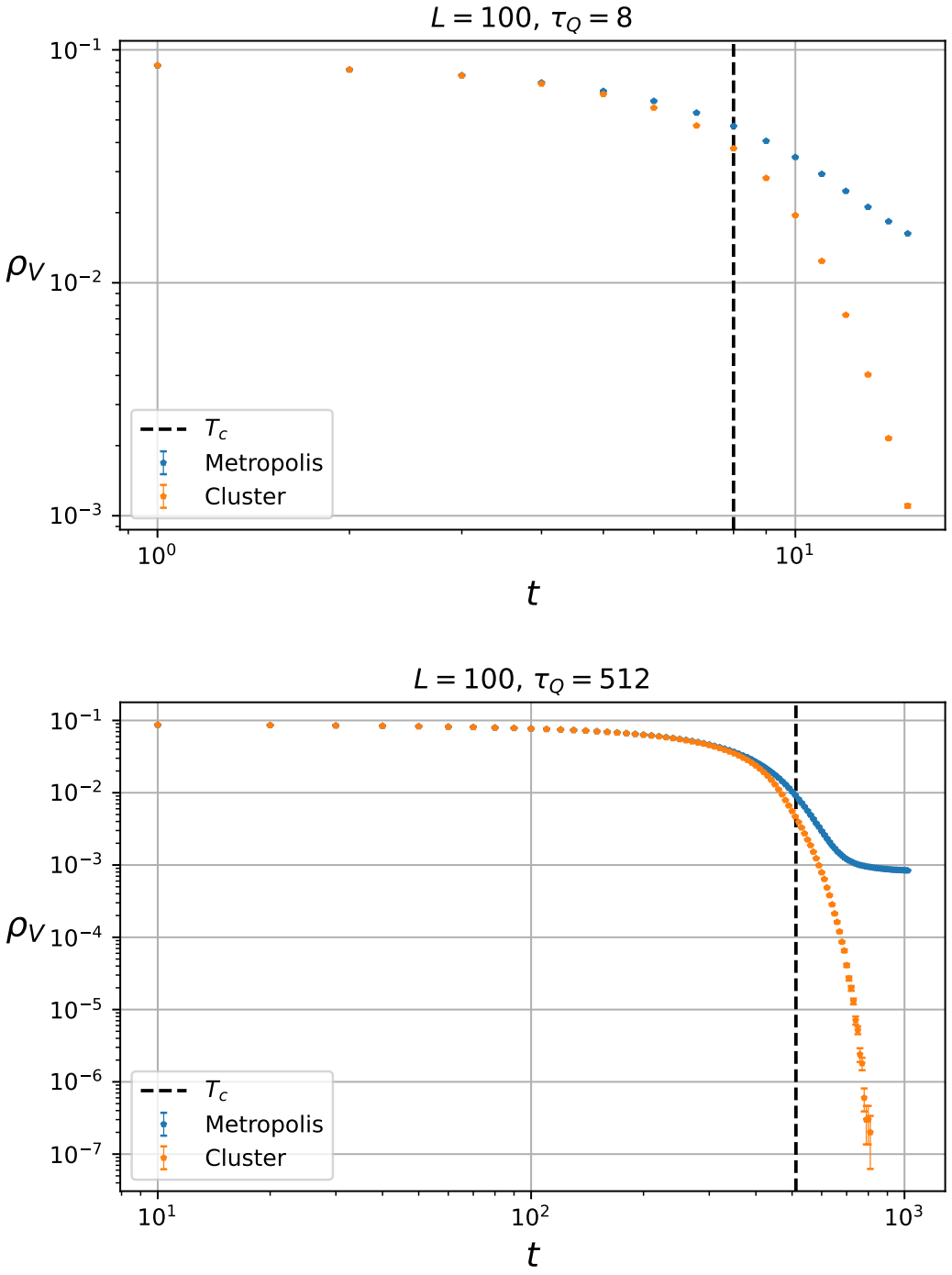

Figure 4.6: Evolution of the density of vortices during a linear quench at different speeds for a 100×100 lattice. A unit of time is given by one sweep, which depends on the algorithm that is used. The upper plot shows a fast quench (τ_Q small), while the lower plot shows a slow quench (τ_Q large). For $t \ll \tau_Q$ we observe that both algorithms coincide. This happens because at the beginning the cooling is adiabatic, but as we get closer to the critical point ($T_c \simeq 0.89$), at a time $t = \tau_Q$, the system leaves equilibrium. Therefore, ρ_V splits depending on the algorithm. Since the cluster algorithm is highly efficient, it tends to equilibrate the system very quickly. As a consequence, ρ_V is close to zero, which is its value in equilibrium at $T = 0$. On the other hand, the Metropolis algorithm is not very efficient, so after the phase transition it does not destroy the vortices as quickly as the cluster algorithm.

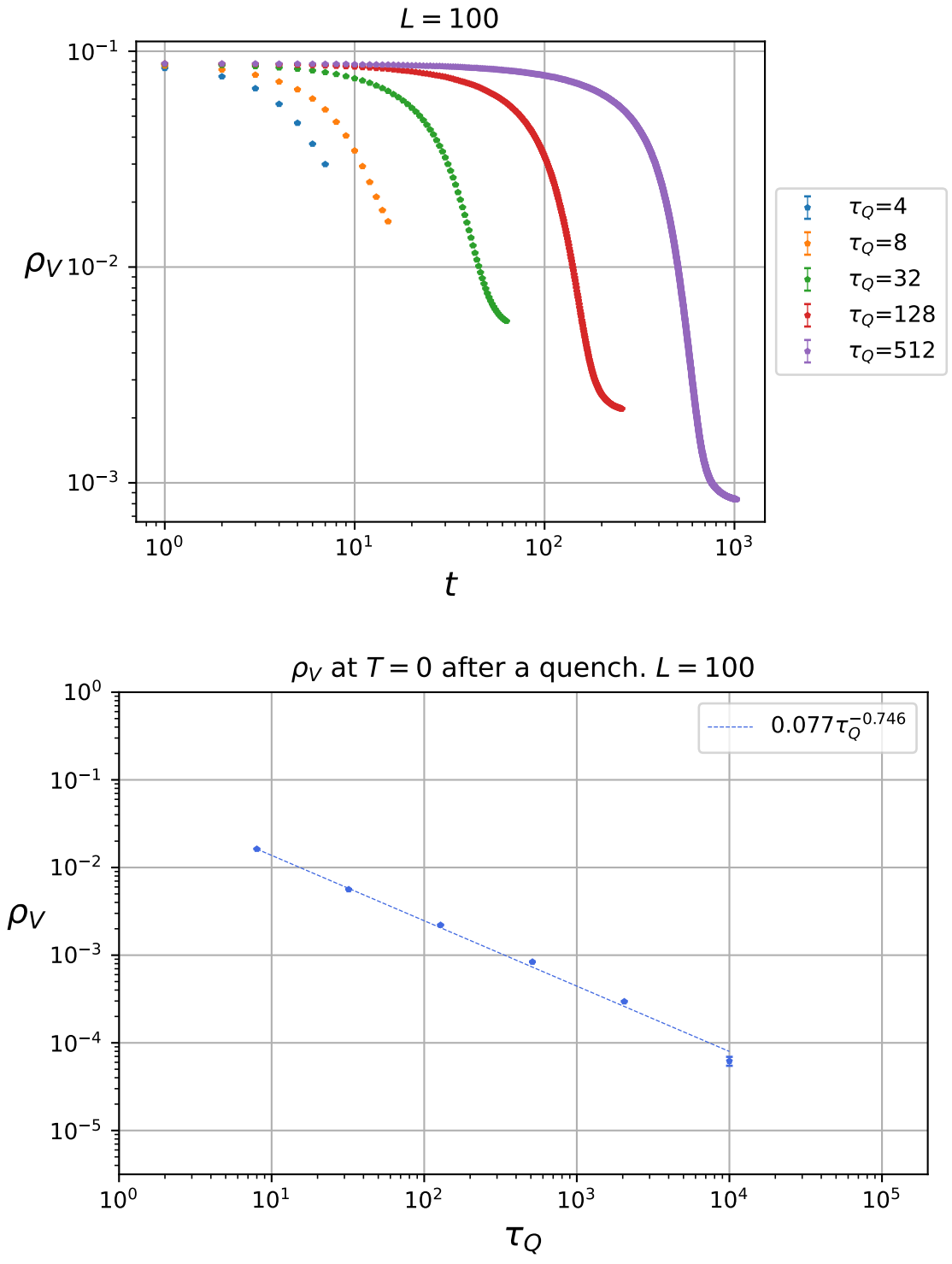

Figure 4.7: The upper plot shows the evolution of the density of vortices for a linear cooling process at different speeds. We worked on a lattice of size 100×100 with the Metropolis algorithm to better preserve some remaining vortices at $T = 0$. The lower figure is a power-law fit to the density of vortices at $T = 0$ as a function of τ_Q. The exponent that we obtain is consistent with the one presented in Figure 14 of Ref. [77].

Chapter 5

3d XY model out of equilibrium

In this chapter we present our simulation results of the 3d XY model out of equilibrium. Again, we are mainly interested in the dynamics of the density of vortices, ρ_V, during a cooling process described by

$$T(t) = T_c \left(1 - \frac{t - \tau_Q}{\tau_Q}\right), \quad t \in [0, 2\tau_Q]. \tag{5.1}$$

Since the model in three dimensions undergoes a second order phase transition, we can test Zurek's prediction for the remnant density of vortices. Now we also use the heatbath algorithm to perform the simulations. This enables us to compare the outcome of the cooling process with two different ways of simulating the evolution out of equilibrium. The objective is to find generic properties that do not depend on the algorithm, which might be compatible with a cooling process in nature.

5.1 Cooling process

In Figure 5.1, we show the evolution of the vortex density during a linear cooling process for a lattice of size $V = 60^3$. In panels (a) and (b) we present a comparison of the dynamics of ρ_V simulated with the Metropolis, heatbath and cluster algorithms. Before the transition we observe that the evolution for the three algorithms coincides, which indicates that the cooling is adiabatic. Close to $t = \tau_Q$, where $T = T_c$,

$$T_c \simeq 2.2018, \tag{5.2}$$

the value of ρ_V splits depending on the algorithm. This indicates the loss of equilibrium. In a similar manner as in two dimensions, the efficiency of the cluster algorithm moves ρ_V to zero at $T = 0$. For the heatbath algorithm, the remnant density after the cooling is below the results of the Metropolis algorithm, but its magnitude is still sufficient to study the dynamics of ρ_V without working with numerical values very close to zero, which could cause trouble.

To test Zurek's prediction for the scaling exponent, we need the density of vortices at $\hat{t}$, *i.e.* at the transition time between the region in equilibrium and the region out of equilibrium, see Figure 1.6. In principle, one could estimate $\hat{t}$ by using eq. (1.40), which we reproduce here for convenience

$$\hat{t} = (C_\tau \tau_Q^{z\nu})^{\frac{1}{1+z\nu}}, \tag{5.3}$$

where C_τ is the proportionality constant between the relaxation time and $1/|T - T_c|^{z\nu}$. As we mentioned in Chapter 3, the relaxation time is related to the exponential autocorrelation time in Monte Carlo simulations. Thus, one could attempt to compute τ in

order to obtain C_τ and determine the exact value of $\hat{t}$. As we have pointed out before, the determination of τ is a difficult task. To avoid computing it, some experiments (see for instance Ref. [6]) measure the density of vortices that remains after cooling from $2T_c$ down to a fixed temperature $T < T_c$, instead of analyzing its value at $\hat{t}$. We expect the scaling behavior of ρ_V in τ_Q, in particular the exponent of the power-law in eq. (1.43), to be independent of the final temperature that we choose. Later we will propose a way of estimating $\hat{t}$ that does not rely on the knowledge C_τ.

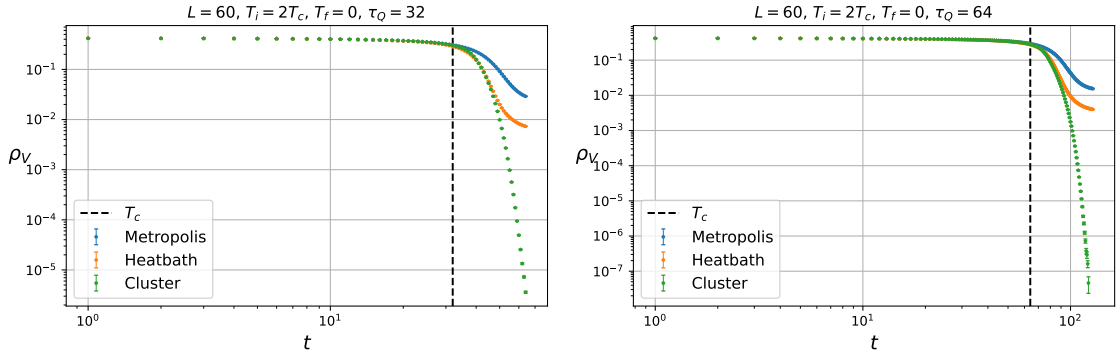

(a)

(b)

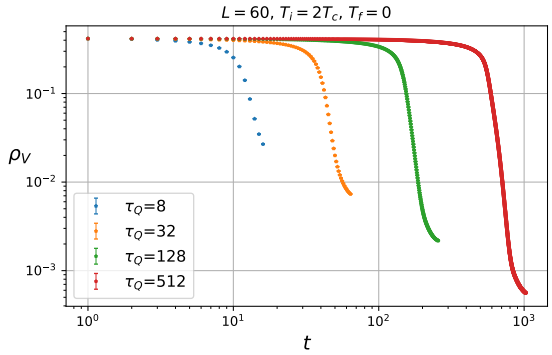

(c) Heatbath algorithm

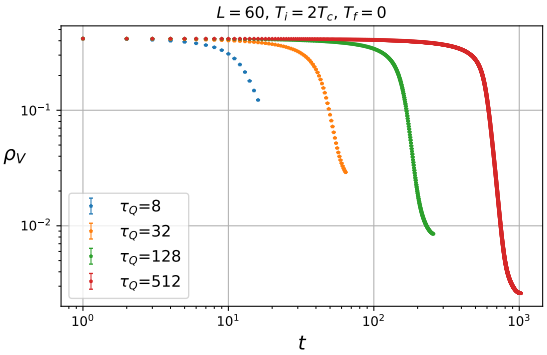

(d) Metropolis algorithm

Figure 5.1: The upper plots show a comparison of the evolution of the density of vortices as simulated by the Metropolis, heatbath and cluster algorithms. We start at $T_i = 2T_c$ and end at $T_f = 0$. As in two dimensions, the cluster algorithm is highly efficient, so it tends to rapidly move ρ_V to its equilibrium value. For the heatbath algorithm the remnant density after the phase transition is below the outcome of the Metropolis algorithm, but it is still useful to study the dynamics out of equilibrium. Close to T_c, the equilibrium is lost and the evolution of ρ_V splits. The lower plots show the cooling process for a fixed algorithm and several τ_Q.

5.2 Testing Zurek's prediction

In this section, we test the prediction by Zurek for the scaling of the density of vortices after a linear cooling process at different values of τ_Q

$$\rho_V \propto \tau_Q^{-2\nu/(1+z\nu)} \equiv \tau_Q^{-\zeta}. \tag{5.4}$$

First, we will study the density of vortices that remains after the cooling process down to some fixed temperature. To be consistent with Zurek's assumptions, we still work with

eq. (5.1), which describes a linear cooling down to zero temperature, starting from $2T_c$. To fix a different final temperature, T_f, we cool the system according to eq. (5.1), but consider the density ρ_V that corresponds to the Markov time t that satisfies $T_f = T(t)$. Since t takes integer values in our simulations, we fix T_f within a tolerance range of 10^{-2}.

In Figure 5.2, we show the density of vortices that remains after cooling down to $T_f \simeq 0.5$, as a function of τ_Q. Simulations were performed by updating random sites. For the Metropolis algorithm we observe that ρ_V as a function of τ_Q follows a power-law behavior to a very high precision. This does not depend on the volume. Thus, the convergence to the infinite volume limit is easily achieved.

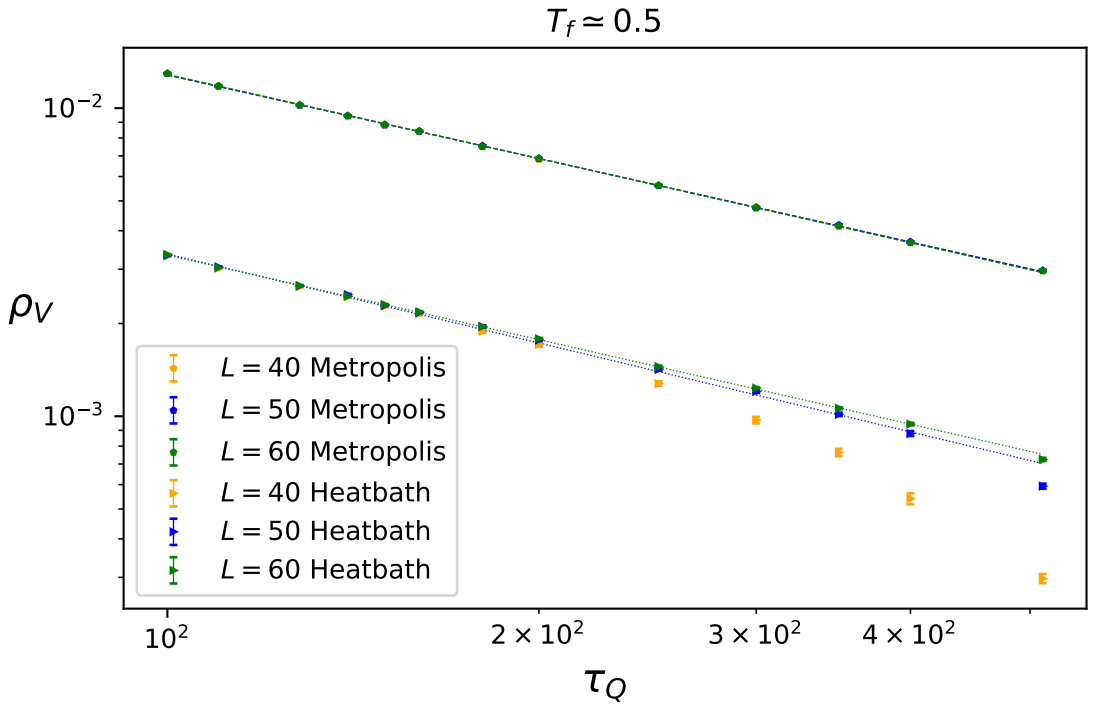

Figure 5.2: Remnant density of vortices at $T_f \simeq 0.5 < T_c$ vs. the inverse cooling rate. For the Metropolis algorithm we observe that the data follow a power-law decay in τ_Q with a high accuracy, independently of the volume. For the heatbath algorithm the results suffer from finite-size effects, so only in large volumes we observe a power-law. We fit functions of the form $\rho_V \propto \tau_Q^{-\zeta}$.

On the other hand, the results of the heatbath algorithm do depend on the volume, which indicates the presence of *finite-size effects*. Furthermore, for small L the data do not obey a power-law, but as we enlarge the volume we see that it tends to follow this behavior. The finite-size effects can be explained by the fact that in a finite volume the relaxation time does not actually diverge at the critical temperature, just like the correlation length. As a consequence, if the algorithm is efficient enough, the observables are shifted towards their value in equilibrium, even after the phase transition. The Metropolis algorithm does not exhibit this effect, which makes it convenient to study the dynamics of a system out of equilibrium. Still, the fact that the remnant density has a power-law behavior in τ_Q, when computed with both algorithms in a large volume, proves that there are universal features of a system out of equilibrium that do not depend on its exact dynamics.

There is no particular reason to choose $T_f \simeq 0.5$ as the final temperature to measure the remnant density of vortices, beyond the fact that $0.5 < T_c$. Thus, one would expect similar results when the system is cooled down to a different temperature, as long as

$T_f < T_c$. In Figures 5.4 and 5.5, we show that this is the case, by presenting ρ_V vs. τ_Q at a final temperature below the critical point in a volume $V = 60^3$. In all cases, a power-law is observed, confirming this behavior as a generic feature of a linear cooling at different speeds. The exact scaling exponents have, however, a dependence on the algorithm and on T_f. In Table 5.1 we display some of the scaling exponents, ζ as defined in eq. (5.4), that we obtain for different final temperatures and for both algorithms. A plot of $\zeta(T_f)$ is shown in Figure 5.3 as well. We can compare them to Zurek's prediction $\zeta = (d - D)\nu/(1 + z\nu)$ by substituting $d = 3$, $D = 1$, $\nu = 0.67169$ and $z = 2$, such that

$$\zeta \simeq 0.5733. \tag{5.5}$$

Our results do not coincide with this exponent. Moreover, the scaling exponents that we found are not constant, although their values are close within the errors in the region $T_f \in [0.001, 0.6]$.

As we mentioned before, Zurek's prediction for ζ is supposed to be valid only at the transition between the region in equilibrium and out of equilibrium, which occurs at some time $\hat{t}$. Thus, the method that we have just presented, which is inspired by the literature [6,77], might not be suitable to test Zurek's prediction. We now propose a way to estimate the value of $\hat{t}$ by analyzing the evolution of the density of vortices. The idea is to determine the time at which the evolution of ρ_V splits for the different algorithms, as shown in Figures 5.1 (a) and (b). We conjecture that this time sets the beginning of the frozen stage or the region out of equilibrium. Notice that this particular time will depend on τ_Q, so the final temperature is not fixed. This method also allows us to use the cluster algorithm, since at $\hat{t}$ the density of vortices is still considerable. To estimate $\hat{t}$, we establish the –arbitrary– condition that the difference in the value of ρ_V, measured with the three algorithms, is greater than 10^{-2}, see Figure 5.6.

By applying this process for various τ_Q, we plot $\rho_V(\hat{t}\,)$ against τ_Q, as shown in Figure 5.7. For all three algorithms, we observe approximately a power-law behavior at $\hat{t}$. However, once again we do not coincide with the scaling exponent ζ that Zurek predicts. Moreover, the scaling exponent does not agree with the ones in Table 5.1 either.

T_f	Metropolis	Heatbath
0.001	0.8705(57)	1.0313(336)
0.01	0.8531(23)	0.9277(117)
0.1	0.8889(34)	0.8734(42)
0.2	0.8952(47)	0.8829(38)
0.3	0.8905(30)	0.8984(58)
0.4	0.8911(22)	0.9103(56)
0.5	0.9073(35)	0.9116(49)
0.6	0.9181(34)	0.9077(43)

Table 5.1: Exponent ζ for the scaling $\rho_V \propto \tau_Q^{-\zeta}$, for which Zurek predicts $\zeta \simeq 0.5733$. We do not coincide with his prediction, although we do observe a power-law behavior. In addition, the dependence of ζ on T_f is not monotonous.

5.3 Interpretation

The results that we presented are in partial agreement with Zurek's work. We do observe a power-law decay for the behavior of the remnant density of vortices as a function of τ_Q, but the exact scaling exponent, ζ, is not the same as he predicts. One possible explanation for this discrepancy could be that $\hat{t}$ is not well determined, but, as we pointed out, it is

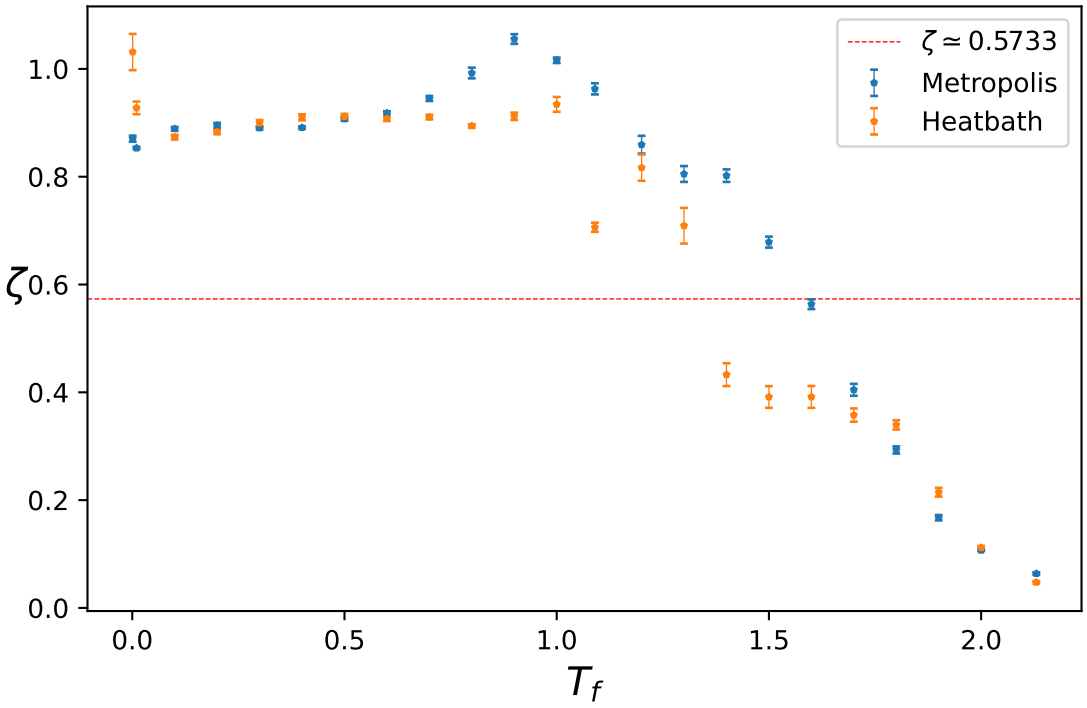

Figure 5.3: Exponent ζ as a function of the final temperature of the cooling for the Metropolis and heatbath algorithms. The data correspond to $V = 60^3$. In the region $T_f \in [0.001, 0.6]$ we observe, in general, good compatibility between the results of both algorithms. For larger values of T_f the results of heatbath become unstable due to the volume. In addition, the behavior of ζ is non-monotonic. We plot the value of Zurek's prediction for comparison.

difficult to carry out this step. Still, it is important that the emergence of power-law is independent of the algorithm that we use. Therefore, the power-law is independent of the exact dynamics of the system, making this property generic.

Experiments that perform a linear cooling process in systems that undergo second order phase transitions also observe this feature, see Refs. [4–6]. The methods that we employ in this thesis can be applied to any model with topological defects. This could be valuable to support the fact that the power-law behavior is indeed generic in a linear cooling.

In addition, it would be of interest to apply these methods to other cosmic strings models to estimate their (hypothetical) density. Even so, to give a proper estimate, one would need to choose an algorithm and a cooling process that matches the dynamics of the early universe. In this work we have used the Metropolis, heatbath and cluster algorithms, together with a linear cooling scheme, to simulate the XY model and we have found generic features. However, we also observed that the exact evolution of ρ_V depends on the particular dynamics of the algorithm. Therefore, to perform simulations out of equilibrium and to use them to compare the outcome with properties of nature, we would need to know the universal features of its dynamics. It could be argued that nature's dynamics is expected to be local and thus a local-update scheme, like Metropolis or heatbath, is adequate. Nonetheless, we saw that the outcome is not exactly the same, although similar. On the other hand, a linear cooling process is not right either, since the cooling of the universe during the expansion was not linear. Further research is needed in these directions.

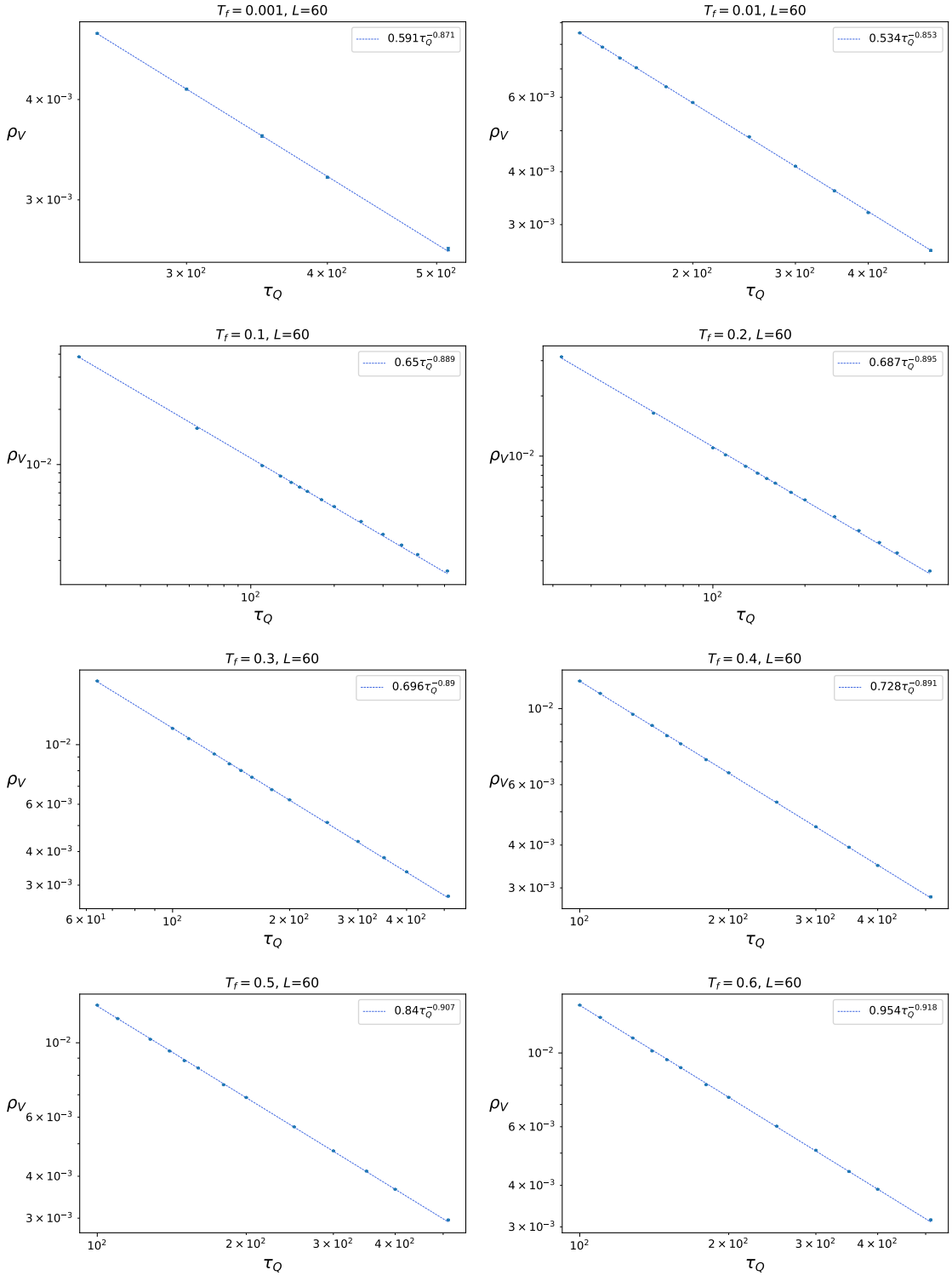

Figure 5.4: Remnant vortex density at different final temperatures after the cooling process. These results were obtained with the Metropolis algorithm. We refer to $L = 60$ and T_f in the range 0.001–0.6.

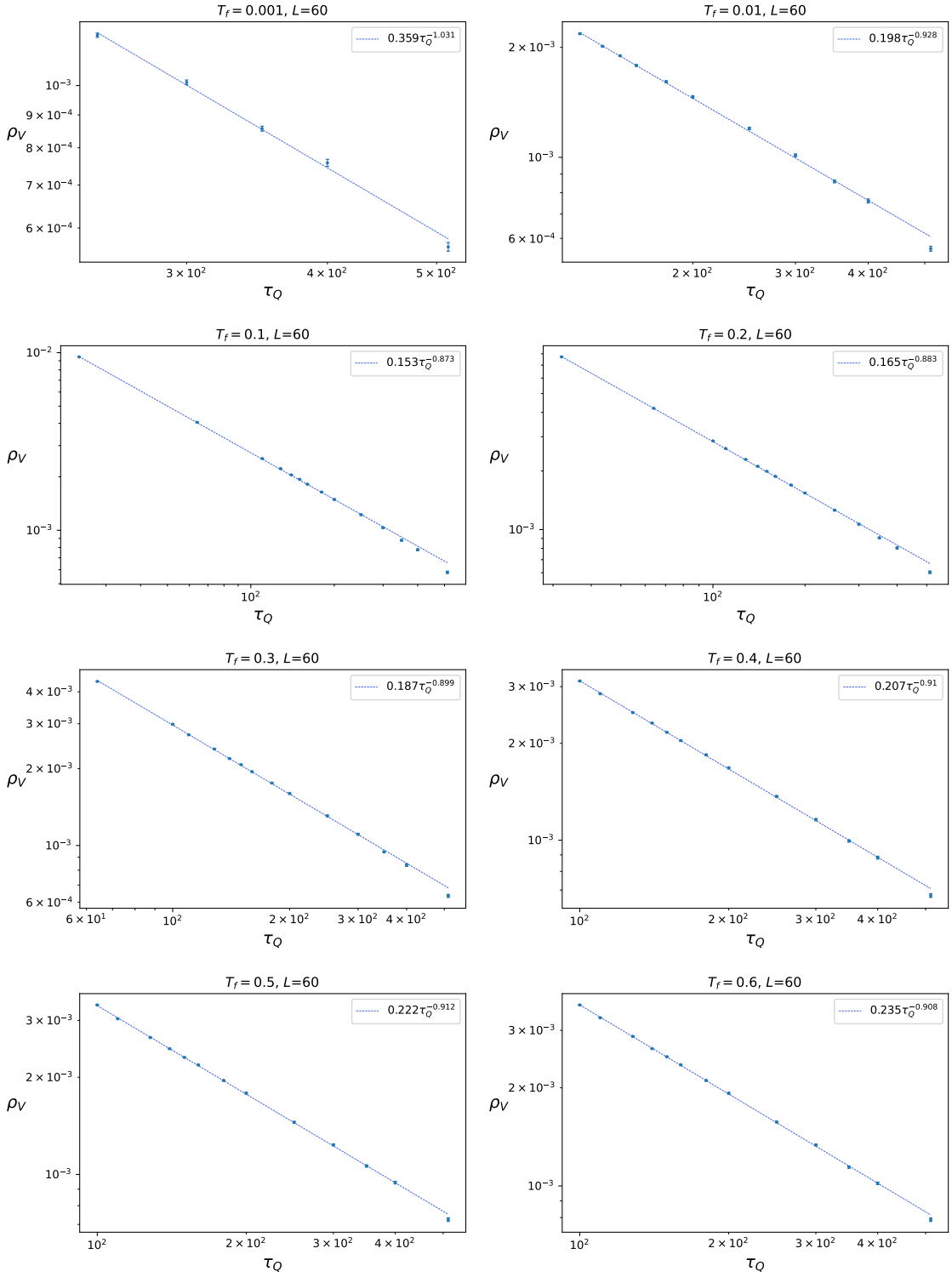

Figure 5.5: Remnant vortex density at different final temperatures after the cooling process. These results were obtained with the heatbath algorithm. We refer to $L = 60$ and T_f in the range 0.001–0.6.

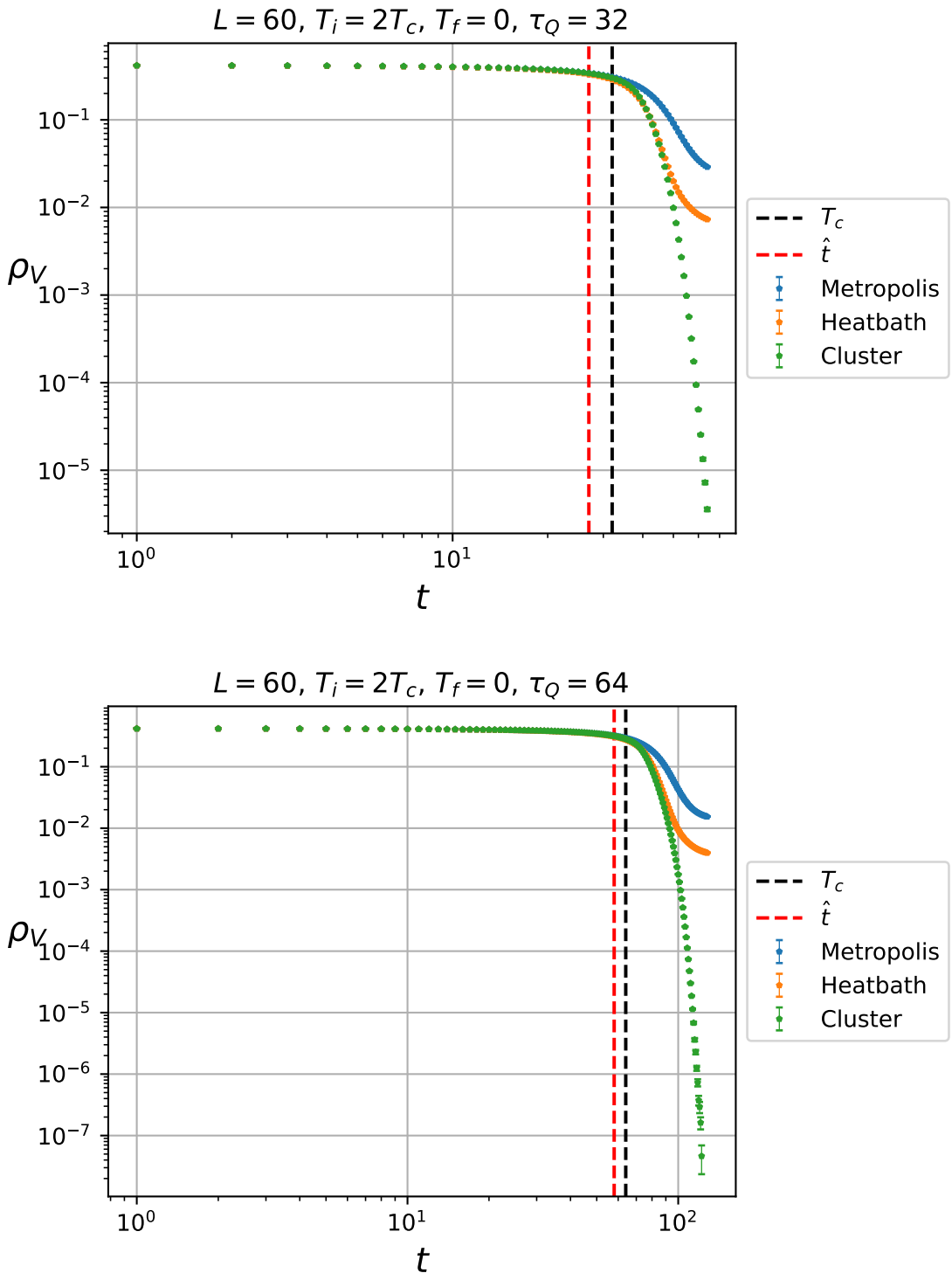

Figure 5.6: We show the estimate of $\hat{t}$ that we obtain by considering the time when the absolute difference of the value of ρ_V measured with the three algorithms is greater than 10^{-2}. We observe that $\hat{t}$ gets closer to the time where the temperature is T_c as we increase τ_Q. This happens because as τ_Q grows the cooling is slower, so the adiabatic stage is longer. For $\tau_Q = 32$ we have $\hat{t} = 27$ and for $\tau_Q = 64$ the value of $\hat{t}$ is 58.

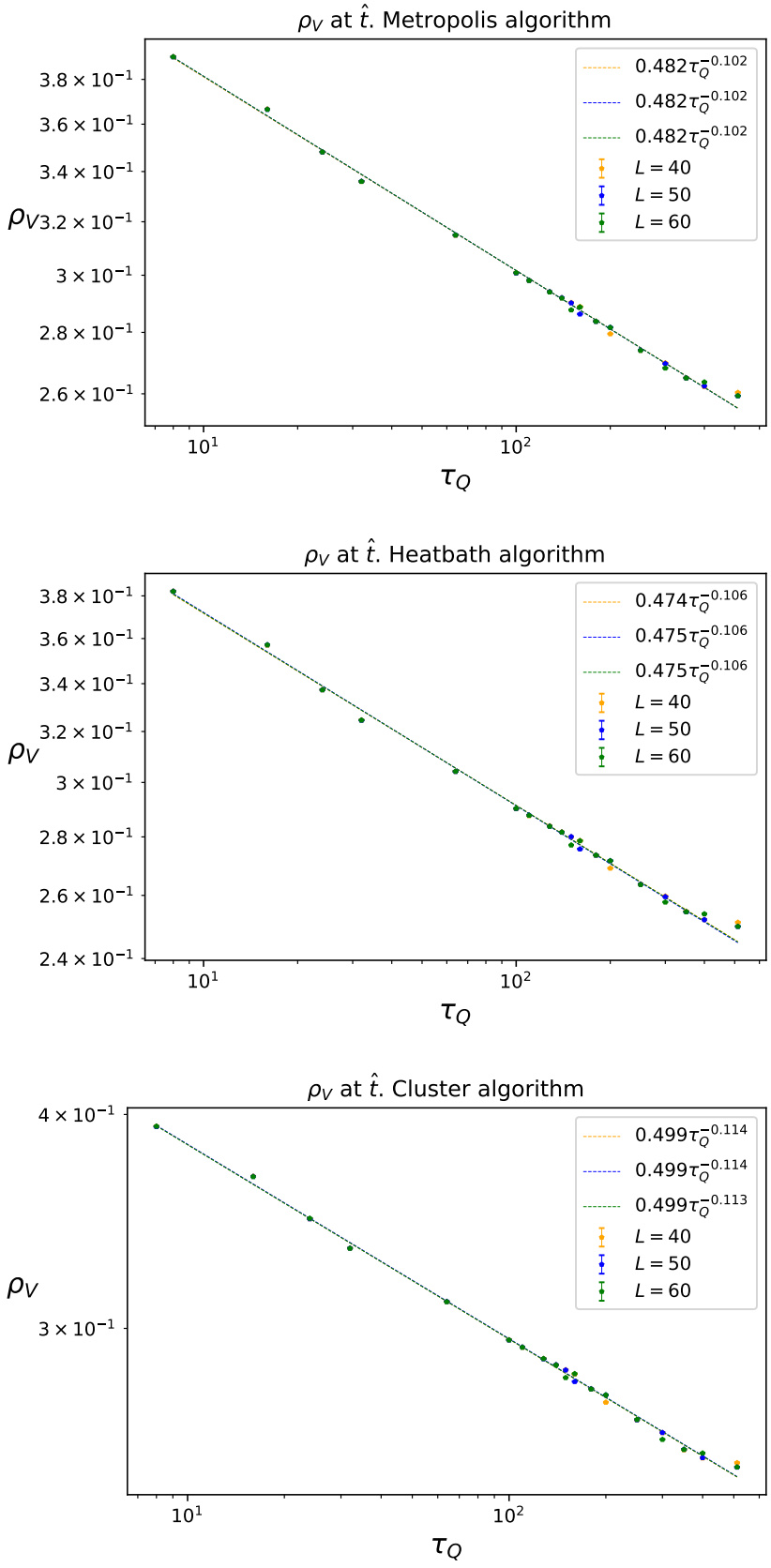

Figure 5.7: Density of vortices at the estimated transition time, $\hat{t}$, between the adiabatic and frozen stages. For all three cases we observe approximately a power-law decay as predicted by Zurek. However, once again the exponent ζ is far away from his prediction for the $z = 2$ case, $\zeta \simeq 0.5733$. Here we do not observe finite-size effects.

Chapter 6

Summary and conclusions

In this thesis we have presented a systematic study of the dynamics of the topological defects of the 2- and 3-dimensional XY model (vortices) when a linear cooling at different rates is applied. To do so, we used Monte Carlo simulations as our tool. The main results were obtained with the Metropolis and heatbath algorithms, which are local-update schemes. Contrary to the case in equilibrium, more efficient algorithms based on collective updates, like the multi-cluster algorithm, are not very practical to study the dynamics out of equilibrium, because they tend to equilibrate the system unrealistically fast. The single-cluster, however, could be useful because it only updates one cluster for each sweep.

Our simulations show that the evolution of the density of vortices during the linear cooling follows a well-defined behavior that is consistent, at least qualitatively, with the dynamics explained by Zurek for a system that undergoes a second order phase transition, see Figure 1.6. A comparison between the results of the three algorithms, Figures 4.5 and 5.1, makes it evident that there are two stages of the cooling process. The first stage corresponds to an adiabatic cooling, where the system is in equilibrium at each instant of time. This can be seen in our results because the three algorithms give the same value for $\rho_V(t)$. The second stage, corresponds to the splitting of ρ_V for each algorithm due to the different increase of the relaxation time. Therefore, at this stage, the evolution of ρ_V depends on the particular dynamics that each algorithm performs. This indicates the loss of equilibrium.

In the 2-dimensional model we confronted our results of the Metropolis algorithm with the ones of Ref. [77]. After a linear cooling starting at $2T_c$, the remnant density of vortices at $T = 0$ indeed follows a power-law decay in τ_Q. The exponent that we obtain for the scaling is $-0.746(13)$, which is compatible with the result of Ref. [77]: -0.72. This comparison shows that the outcome of our implementations is consistent with previous results in the literature, which encouraged us to apply the same method to the 3-dimensional XY model, where no simulations out of equilibrium had been performed. We remark that for the 2-dimensional model, Zurek's prediction for the scaling of the density of topological defects is not intended, because the transition is not second order, but instead topological. It is still interesting that the behavior of ρ_V after the cooling is similar.

To test Zurek's prediction for the scaling of ρ_V with τ_Q, we studied the 3-dimensional XY model. In this case we performed a systematic study by using the Metropolis and heatbath algorithm and by analyzing the results in different volumes. The remnant density of vortices at a final temperature $T_f < T_c$ (after the cooling) behaves indeed as a power-law in τ_Q, as shown in Figures 5.4 and 5.5. We found this feature to be independent of the final temperature that one chooses for the cooling. Moreover, for large volumes this

property is observed both with the Metropolis and heatbath algorithms. Thus, based on our results, we conclude that the power-law behavior for the remnant density is a generic property that does not depend on the exact dynamics of the system. In addition, recent work [78] suggests that this feature does not depend on whether or not a phase transition occurs, like in the 1d Ising or XY model, where no phase transition is exhibited.

However, the exact scaling, given by the exponent ζ, shows a slight dependence on the algorithm and the final temperature that we fix to do the cooling (see Table 5.1). Furthermore, our values for ζ do not coincide with the prediction by Zurek, $\zeta \simeq 0.5733$, for the particular model that we studied. This discrepancy could be associated to the fact that Zurek's prediction is actually valid for the time $\hat{t}$, where the transition between the adiabatic and frozen stages occurs. Still, Zurek's prediction has been successfully tested in experiments by measuring only the density of topological defects at a final fixed temperature after the cooling, see *e.g.* Ref. [6], but no $\hat{t}$ is specified. We proposed a way to estimate the value of $\hat{t}$ by analyzing the evolution of ρ_V and determining the time at which its dynamics splits for each algorithm. Then, we studied once more the behavior of ρ_V as a function of τ_Q and found an approximate power-law behavior. Nevertheless, the scaling exponent does not agree with Zurek's value for ζ either. Thus, our results only show a partial agreement with his prediction. Better precision requires to measure τ_{exp}. The objective would be to determine τ_{exp}, for several values of T, in equilibrium in order to fit a power-law to obtain with precision the dynamical critical exponent z and C_τ, as shown in eq. (1.40). That way, the estimation of $\hat{t}$ should be precise and Zurek's prediction for the exponent ζ can be better tested.

This work could continue in different directions. First, one can apply the same method to other simple models that undergo second order phase transitions, in order to verify whether the power-law behavior is universal. This type of studies have been done already with simulations in different systems (see *e.g.* Refs. [6, 79]), but not in a systematic way, *i.e.* for different volumes and algorithms as in this work.

Extensions of the Kibble-Zurek mechanism exist [80]. They provide predictions for the scaling behavior of the density of topological defects as a function of τ_Q at arbitrary times t during the linear cooling, not necessarily at $\hat{t}$. This could be further tested in different models.

One could take the next step and apply this method to a gauge theory with cosmic strings as topological defects, for instance the Abelian Higgs model (Nielsen-Olesen strings). This could be useful to estimate the remnant density of cosmic strings in the universe. Finally, it is yet open question which cooling schemes and algorithms are appropriate to simulate nature out of equilibrium. As for now, the universal property that we observed is limited to a power-law.

References

[1] T. W. B. Kibble. Topology of cosmic domains and strings. *J. Phys. A*, **9**:1387, (1976).

[2] P. Auclair et al. Probing the gravitational wave background from cosmic strings with LISA. *J. Cosmol. Astropart. Phys.*, **04**:034, (2020).

[3] W. H. Zurek. Cosmological experiments in superfluid helium? *Nature*, **317**:505–508, (1985).

[4] S. Ducci, P. L. Ramazza, W. González-Viñas and F. T. Arecchi. Order Parameter Fragmentation after a Symmetry-Breaking Transition. *Phys. Rev. Lett.*, **83**:5210–5213, (1999).

[5] S. Casado, W. González-Viña, H. Mancini and S. Boccaletti. Topological defects after a quench in a Bénard-Marangoni convection system. *Phys. Rev. E*, **63**:057301, (2001).

[6] S.-Z. Lin et al. Topological defects as relics of emergent continuous symmetry and Higgs condensation of disorder in ferroelectrics. *Nat. Phys.*, **10**:970–977, (2014).

[7] M. Hindmarsh, M. Lüben, J. Lumma and M. Pauly. Phase transitions in the early universe. *SciPost Phys. Lect. Notes*, (2021).

[8] L. Dolan and R. Jackiw. Symmetry behavior at finite temperature. *Phys. Rev. D*, **9**:3320–3341, (1974).

[9] A. Das. *Finite Temperature Field Theory*. World Scientific, first edition, (1997).

[10] N. D. Mermin. The topological theory of defects in ordered media. *Rev. Mod. Phys.*, **51**:591, (1979).

[11] I. Y. Kobsarev, L. B. Okun and Y. B. Zeldovich. Spontaneus [sic] CP-violation and cosmology. *Phys. Lett. B*, **50**:340–342, (1974).

[12] A. M. Polyakov. Particle Spectrum in Quantum Field Theory. *JETP Lett.*, **20**:194–195, (1974).

[13] G. 't Hooft. Magnetic monopoles in unified gauge theories. *Nucl. Phys. B*, **79**:276–284, (1974).

[14] M. Daniel, G. Lazarides and Q. Shafi. SU(5) monopoles, magnetic symmetry and confinement. *Nucl. Phys. B*, **170**:156–164, (1980).

[15] H. Fritzsch and P. Minkowski. Unified Interactions of Leptons and Hadrons. *Ann. Phys.*, **93**:193–266, (1975).

[16] J. P. Preskill. Cosmological Production of Superheavy Magnetic Monopoles. *Phys. Rev. Lett.*, **43**:1365, (1979).

[17] H. B. Nielsen and P. Olesen. Vortex-line models for dual strings. *Nucl. Phys. B*, **61**:45–61, (1973).

[18] M. B. Hindmarsh and T. W. B. Kibble. Cosmic strings. *Rep. Prog. Phys.*, **58**:477, (1995).

[19] T. Charnock, A. Avgoustidis, E. J. Copeland and A. Moss. CMB constraints on cosmic strings and superstrings. *Phys. Rev. D*, **93**:123503, (2016).

[20] M. J. White and D. Scott. The Impact of the Cosmic Microwave Background on Large-Scale Structure. *Comments Astrophys.*, **18**:289, (1996).

[21] A. Albrecht, R. A. Battye and J. Robinson. The Case against Scaling Defect Models of Cosmic Structure Formation. *Phys. Rev. Lett.*, **79**:4736–4739, (1997).

[22] U.-L. Pen, U. Seljak and N. Turok. Power Spectra in Global Defect Theories of Cosmic Structure Formation. *Phys. Rev. Lett.*, **79**:1611–1614, (1997).

[23] M. Wyman, L. Pogosian and I. Wasserman. Bounds on cosmic strings from WMAP and SDSS. *Phys. Rev. D*, **72**:023513, (2005).

[24] A. Vilenkin and E. P. S. Shellard. *Cosmic Strings and Other Topological Defects.* Cambridge University Press, first edition, (1994).

[25] A. Gangui. Topological Defects in Cosmology. Lecture Notes for the First Bolivian School on Cosmology, (2001).

[26] D. S. Gorbunov and V. A. Rubakov. *Introduction to the Theory of the Early Universe.* World Scientific, first edition, (2011).

[27] A. del Campo and W. H. Zurek. Universality of phase transition dynamics: Topological defects from symmetry breaking. *Int. J. Mod. Phys. A*, **29**:1430018, (2014).

[28] T. W. B. Kibble. Phase-transition dynamics in the lab and the universe. *Phys. Today*, **60**:47, (2007).

[29] D. R. Nelson and J. M. Kosterlitz. Universal Jump in the Superfluid Density of Two-Dimensional Superfluids. *Phys. Rev. Lett.*, **39**:1201–1205, (1977).

[30] K. K. Mon and W. F. Saam. Two-layer XY model for ^{4}He films. *Phys. Rev. B*, **22**:3221–3229, (1980).

[31] N. Schultka and E. Manousakis. Crossover from two- to three-dimensional behavior in superfluids. *Phys. Rev. B*, **51**:11712–11720, (1995).

[32] N. Schultka and E. Manousakis. Specific heat of superfluids near the transition temperature. *Phys. Rev. B*, **52**:7528–7536, (1995).

[33] V. L. Berezinskiĭ. Destruction of long range order in one-dimensional and two-dimensional systems having a continuous symmetry group. I. Classical systems. *Sov. Phys. JETP*, **32**:493–500, (1971).

[34] V. L. Berezinskiĭ. Destruction of Long-range Order in One-dimensional and Two-dimensional Systems Possessing a Continuous Symmetry Group. II. Quantum Systems. *Sov. Phys. JETP*, **34**:610, (1972).

[35] J. M. Kosterlitz and D. J. Thouless. Ordering, metastability and phase transitions in two-dimensional systems. *J. Phys. C: Solid State Phys.*, **6**:1181, (1973).

[36] N. D. Mermin and H. Wagner. Absence of ferromagnetism or antiferromagnetism in one-dimensional or two-dimensional isotropic Heisenberg models. *Phys. Rev. Lett.*, **17**:1133–1136, (1966).

[37] The Royal Swedish Academy of Sciences. Topological phase transitions and topological phases of matter. https://www.nobelprize.org/uploads/2018/06/advanced-

physicsprize2016-1.pdf, (2016).

[38] W. Bietenholz and U. Gerber. Berezinskiĭ-Kosterlitz-Thouless Transition and the Haldane Conjecture: Highlights of the Physics Nobel Prize 2016. *Rev. Cub. Fis.*, **33**:156, (2016).

[39] M. Kardar. *Statistical Physics of Fields.* Cambridge Univeristy Press, first edition, (2007).

[40] A. V. Pochinsky, M. I. Polikarpov and B. N. Yurchenko. Properties of vortex loops in the 3D XY model. *Phys. Lett. A*, **154**:194–196, (1991).

[41] A. Hulsebos. The behavior of vortex loops in the 3-d XY model. *Nucl. Phys. B Proc. Suppl.*, **34**:695–697, (1994).

[42] K. Kajantie, M. Laine, T. Neuhaus, A. Rajantie and K. Rummukainen. O(2) symmetry breaking versus vortex loop percolation. *Phys. Lett. B*, **482**:114–122, (2000).

[43] M. Campostrini, M. Hasenbusch, A. Pelissetto and E. Vicari. Theoretical estimates of the critical exponents of the superfluid transition in ^{4}He by lattice methods. *Phys. Rev. B*, **74**:144506, (2006).

[44] M. Hasenbusch. Monte Carlo study of an improved clock model in three dimensions. *Phys. Rev. B*, **100**:224517, (2019).

[45] P. M. Chaikin and T. C. Lubensky. *Principles of condensed matter physics.* Cambridge University Press, first edition, (1995).

[46] H. Nishimori and G. Ortiz. *Elements of Phase Transitions and Critical Phenomena.* Oxford Graduate Texts. Oxford University Press, first edition, (2011).

[47] K. L. Chung. *Markov Chains with Stationary Transition Probabilities.* Grundlehren der mathematischen Wissenschaften. Springer, (1960).

[48] B. A. Berg. *Markov Chain Monte Carlo Simulations and Their Statistical Analysis.* World Scientific, first edition, (2004).

[49] A. Sokal. *Monte Carlo Methods in Statistical Mechanics: Foundations and New Algorithms.* In: Functional Integration, C. DeWitt-Morette and A. Folacci (Editors), Springer, (1997).

[50] J. Salas and A. D. Sokal. Dynamic critical behavior of the Swendsen-Wang algorithm: The two-dimensional three-state Potts model revisited. *J. Stat. Phys.*, **87**:1–36, (1997).

[51] W. Janke. Nonlocal Monte Carlo algorithms for statistical physics applications. *Math. Comput. Simul.*, **47**:329–346, (1998).

[52] W. Janke. *Monte Carlo Simulations of Spin Systems. In: K. H. Hoffmann and M. Schreiber (eds).* Springer, (1996).

[53] H. J. Rothe. *Lattice Gauge Theories.* World Scientific Lecture Notes in Physics. World Scientific, fourth edition, (2012).

[54] C. Gattringer and C. B. Lang. *Quantum Chromodynamics on the Lattice: An Introductory Presentation.* Lect. Notes Phys. Springer, first edition, (2010).

[55] J. F. Nieto Castellanos. O-2-Model. https://github.com/Fabian2598/O-2-Model, (2023).

[56] N. Metropolis, A. W. Rosenbluth, M. N. Rosenbluth, A. H. Teller and E. Teller. Equation of State Calculations by Fast Computing Machines. *J. Chem. Phys.*, **21**:1087–

1092, (1953).

[57] M. Creutz and B. Freedman. A Statistical Approach to Quantum Mechanics. *Ann. Phys.*, **132**:427–462, (1981).

[58] C. Münkel, D. W. Heermann, J. Adler, M. Gofman and D. Stauffer. The dynamical critical exponent of the two-, three- and five-dimensional kinetic Ising model. *Phys. A: Stat. Mech.*, **193**:540–552, (1993).

[59] M. Hasenbusch. Dynamic critical exponent z of the three-dimensional Ising universality class: Monte Carlo simulations of the improved Blume-Capel model. *Phys. Rev. E*, **101**:022126, (2020).

[60] R. H. Swendsen and J.-S. Wang. Nonuniversal critical dynamics in Monte Carlo simulations. *Phys. Rev. Lett.*, **58**:86–88, (1987).

[61] U. Wolff. Collective Monte Carlo Updating for Spin Systems. *Phys. Rev. Lett.*, **62**:361–364, (1989).

[62] J. Hoshen and R. Kopelman. Percolation and cluster distribution. I. Cluster multiple labeling technique and critical concentration algorithm. *Phys. Rev. B*, **14**:3438–3445, (1976).

[63] M. Hasenbusch and S. Meyer. Critical exponents of the 3D XY model from cluster update Monte Carlo. *Phys. Lett. B*, **241**:238–242, (1990).

[64] M. Dilaver, S. Gündüç, M. Aydın and Y. Gündüç. Dynamic critical index of the Swendsen–Wang algorithm by dynamic finite-size scaling. *Comput. Phys. Commun.*, **175**:553–558, (2006).

[65] M. Creutz. Monte Carlo study of quantized SU(2) gauge theory. *Phys. Rev. D*, **21**:2308–2315, (1980).

[66] E. Pietarinen. String tension in SU(3) lattice gauge theory. *Nucl. Phys. B*, **190**:349–356, (1981).

[67] N. Cabibbo and E. Marinari. A new method for updating SU(N) matrices in computer simulations of gauge theories. *Phys. Lett. B*, **119**:387–390, (1982).

[68] Y. Miyatake, M. Yamamoto, J. J. Kim, M. Toyonaga and O. Nagai. On the implementation of the 'heat bath' algorithms for Monte Carlo simulations of classical Heisenberg spin systems. *J. Phys. C: Solid State Phys.*, **19**:2539, (1986).

[69] S. G. Pawig and K. Pinn. Monte Carlo Algorithms for the Fully Frustrated XY Model. *Int. J. Mod. Phys. C*, **09**:727–736, (1998).

[70] T. Hattori and H. Nakajima. Improvement of efficiency in generating random $U(1)$ variables with Boltzmann distribution. *Nucl. Phys. B Proc. Suppl.*, **26**:635–637, (1992).

[71] N. Prokof'ev and B. Svistunov. Worm Algorithms for Classical Statistical Models. *Phys. Rev. Lett.*, **87**:160601, (2001).

[72] C. Gattringer. New developments for dual methods in lattice field theory at non-zero density. *PoS*, **LATTICE2013**:002, (2014).

[73] D. Göschl, C. Gattringer, A. Lehmann and C. Weis. Simulation strategies for the massless lattice Schwinger model in the dual formulation. *Nucl. Phys. B*, **924**:63–85, (2017).

[74] M. Hasenbusch. The two-dimensional XY model at the transition temperature: a high-precision Monte Carlo study. *J. Phys. A: Math. Gen.*, **38**:5869, (2005).

[75] R. G. Jha. Critical analysis of two-dimensional classical XY model. *J. Stat. Mech. Theory Exp.*, **2020**:083203, (2020).

[76] S. G. Chung. Essential finite-size effect in the two-dimensional XY mode. *Phys. Rev. B*, **60**:11761, (1999).

[77] A. Jelić and L. F. Cugliandolo. Quench dynamics of the 2d XY model. *J. Stat. Mech. Theory Exp.*, **2011**:P02032, (2011).

[78] J. A. Pérez Loera. Evolución de fronteras de dominio en el modelo de Ising durante un enfriamiento fuera del equilibrio, B.Sc. thesis, Universidad Nacional Autónoma de México, in preparation.

[79] M. Hindmarsh and A. Rajantie. Defect Formation and Local Gauge Invariance. *Phys. Rev. Lett.*, **85**:4660, (2000).

[80] G. Biroli, L. F. Cugliandolo and A. Sicilia. Kibble-Zurek mechanism and infinitely slow annealing through critical points. *Phys. Rev. E*, **81**:050101, (2010).